

Optical detectors for focal plane arrays^{*}

A. ROGALSKI^{*}

Institute of Applied Physics, Military University of Technology
2 Kaliskiego Str., 00-908 Warsaw, Poland

The paper presents progress in optical detector technologies during the past 25 years. Classification of two types of detectors (photon detectors and thermal detectors) is done on the basis of their principle of operation. The overview of optical material systems and detectors is presented. Also recent progress in different technologies is described. Discussion is focused mainly on current and the most rapidly developing focal plane arrays using: CdZnTe detectors, AlGaIn photodiodes, visible CCD and CMOS imaging systems, HgCdTe heterostructure photodiodes, quantum well AlGaAs/GaAs photoresistors, and thermal detectors. The outlook for near-future trends in IR technologies is also presented.

Keywords: photon detectors, thermal detectors, optical detectors, focal plane arrays, multi-colour detectors.

1. Introduction

Looking back over the past several hundreds of years we noticed that following the invention and evolution of optical systems (telescopes, microscopes, eyeglasses, cameras, etc.), the optical image was still formed on the human retina, photographic plate, or films. The birth of photodetectors can be dated back to 1873 when Smith discovered photoconductivity in selenium. Progress was slow until 1905, when Einstein explained the newly observed photoelectric effect in metals, and Planck solved the blackbody emission puzzle by introducing the quanta hypothesis. Applications and new devices soon flourished, pushed by the dawning technology of vacuum tube sensors developed in the 1920s and 1930s culminating in the advent of television. Zworykin and Morton, the celebrated fathers of videonics, on the last page of their legendary book *Television* (1939) concluded that: “when rockets will fly to the moon and to other celestial bodies, the first images we will see of them will be those taken by camera tubes, which will open to mankind new horizons”. Their foresight became a reality with the Apollo and Explorer missions. Photolithography enabled the fabrication of silicon monolithic imaging focal planes for the visible spectrum beginning in the early 1960s. Some of these early developments were intended for a picturephone, other efforts were for television cameras, satellite surveillance, and digital imaging. Infrared imaging has been vigorously pursued in parallel with visible imaging because of its utility in military applications. More recently (1997), the CCD camera aboard the

Hubble space telescope delivered a deep-space picture, a result of 10 day’s integration, featuring galaxies of the 30th magnitude – an unimaginable figure even for astronomers of our generation. Probably, the next effort will be in the big-band age. Thus, photodetectors continue to open to mankind the most amazing new horizons.

This paper is a guide over the arrays of detectors sensing optical radiation. Optical radiation is considered as a radiation over the range from vacuum ultraviolet to the far-infrared or submillimeter wavelength (25 nm to 1000 μ m):

25–200 nm	Vacuum ultraviolet	VUV
200–400 nm	Ultraviolet	UV
400–700 nm	Visible	VIS
700–1000 nm	Near infrared	NIR
1–3 μ m	Short wavelength infrared	SWIR
3–5 μ m	Medium wavelength infrared	MWIR
5–14 μ m	Long wavelength infrared	LWIR
14–30 μ m	Very long wavelength infrared	VLWIR
30–100 μ m	Far infrared	FIR
100–1000 μ m	Submillimeter	SubMM

2. Classification of detectors

Progress in optical detector technology is connected mainly with semiconductor IR detectors which are included in the class of photon detectors. In this class of detectors, the radiation is absorbed within the material by interaction with electrons. The observed electrical output signal results from the changed electronic energy distribution. The photon detectors show a selective wavelength dependence of the response per unit incident radiation power. They exhibit both perfect signal-to-noise performance and a very fast response. However, to achieve this in infrared (IR) spectral region, the photon de-

^{*}e-mail: rogan@wat.edu.pl

^{*}This paper was presented during the XVII School of Optoelectronics: Photovoltaics-Solar Cells and Detectors, Kazimierz Dolny, October 13–17, 2003.

tectors require cryogenic cooling. Cooling requirements are the main obstacle to the more widespread use of IR systems based on semiconductor photodetectors making them bulky, heavy, expensive and inconvenient to use. Depending on the nature of interaction, the class of photon detectors is further sub-divided into different types (see Table 1). The most important are: intrinsic detectors, extrinsic detectors, photoemissive (metal silicide Schottky barriers) detectors, and quantum well detectors.

The second class of detectors is composed of thermal detectors. In a thermal detector, the incident radiation is absorbed to change temperature of the material, and the resultant change in some physical properties is used to generate an electrical output. The detector element is suspended on lags which are connected to the heat sink. Thermal effects are generally wavelength independent; the signal depends upon the radiant power (or its rate of change) but not upon its spectral content. In pyroelectric detectors a change in the internal spontaneous polarization is measured, whereas in the case of bolometers a change in the electrical resistance is measured. The thermal detectors typically operate at room temperature. They are usually characterized by modest sensitivity and slow response but they are cheap and easy to use. The greatest utility in infrared technology has found bolometers, pyroelectric detectors and thermopiles.

Up till the nineties last century, thermal detectors have been considerably less exploited in commercial and military infrared systems in comparison with photon detectors. The reason for this disparity is that thermal detectors were popularly believed to be rather slow and insensitive in comparison with photon detectors. As a result, the worldwide effort to develop thermal detectors was extremely small relative to that of photon detector. In the last decade, however, it has been shown that extremely good imagery can be obtained from large thermal detector arrays operating uncooled at TV frame rates. The speed of thermal detectors is quite adequate for non-scanned imagers with two-dimensional (2D) detectors. The moderate sensitivity of thermal detectors can be compensated by a large number of elements in 2D electronically scanned arrays. With large arrays of thermal detectors the best values of temperature

resolution below 0.1 K is reached because effective noise bandwidths less than 100 Hz can be achieved.

3. Performance specifications

To provide easy comparison between detectors, certain figures of merit, computed from the measured data, have been defined.

The voltage (or analogous current) responsivity is given by

$$R = \frac{Q_u}{P}, \quad (1)$$

where Q_u is the output quantity supplied by the detector (e.g., the current I_u , the voltage V_u , or any other physical quantity) and P is the incident radiant power.

At equal responsivity, the detector with the smallest output noise Q_u on the useful signal is the most sensitive. Therefore, the first figure of merit for a detector is the NEP – noise equivalent power defined as the ratio of output noise to responsivity

$$NEP = \frac{S_n}{R}. \quad (2)$$

So, the NEP represents the input power that gives a unity signal to noise ratio, $S/N = 1$ at the output; that is, a marginal condition of detection.

The better the detector performance is, since the smaller the NEP is. Therefore it is more convenient to define its inverse as a merit figure. In addition, it should be taken into consideration that whatever the noise source is, it can be expected that the noise quadratic total value is proportional to observation bandwidth Δf and the detector area A . Thus, is even better to take, as the intrinsic noise parameter of a detector, the ratio $NEP/(A\Delta f)^{1/2}$ normalized to unit area and bandwidth. In order to simplify the comparison of different detectors and to have a parameter that increases as the performance improves, the detectivity D^* (called *D-star*) is defined as

$$D^* = \frac{(A\Delta f)^{1/2}}{NEP}. \quad (3)$$

Table 1. Photon detectors.

Type	Transition	Electrical output	Example
Intrinsic	Interband	Photoconductive Photovoltaic Capacitance PEM	AlGaIn, Si, GaAs, PbSe, InSb, HgCdTe AlGaIn, Si, InGaAs, InSb, HgCdTe Si, GaAs, InSb, HgCdTe InSb, HgCdTe
Extrinsic	Impurity to band	Photoconductive	Si:In, Si:Ga, Ge:Cu, Ge:Hg
Free carriers	Intraband	Photoemissive Photoconductive Photon-drag	PtSi, Pt ₂ Si, IrSi Schottky barriers GaAs/CsO InSb electron bolometer Ge
Quantum wells	To and/or from spatially quantised levels	Photoconductive Photovoltaic	GaAs/GaAlAs, InSb <i>nipi</i> InAs/InGaSb SLS

This is the fundamental figure of merit used for detectors. It can be transformed to the following equation

$$D^* = \frac{(A\Delta f)^{1/2}}{P} \frac{S}{N}. \quad (4)$$

The ultimate performance of detectors is reached when the detector and amplifier noise is low compared to the photon noise. The photon noise is fundamental in the sense that it arises not from imperfection in the detector or its associated electronics but rather from the detection process itself, as a result of the discrete nature of the radiation field. The radiation falling on the detector is a composite of that from the target and that from the background.

When photodetectors are operated in conditions where the background flux is less than the optical (signal) flux, the ultimate performance of detectors is determined by the signal fluctuation limit (*SFL*). It is achieved in practice with photomultipliers operating in the visible and ultraviolet region, but it is rarely achieved with solid-state devices, which are normally detector-noise or electronic noise limited. The *NEP* of detectors operating in this limit have been derived by a number of authors (see e.g. Kruse *et al.* [1,2]).

The *NEP* in the *SFL* is given (when Poisson statistics are applicable) by

$$NEP = \frac{2hc\Delta f}{\eta\lambda}, \quad (5)$$

where h is the Planck's constant, c is the light velocity, η is the quantum efficiency, and λ is the wavelength.

The practical operating limit for most infrared detectors is not the *SFL* but the background fluctuation limit, also known as the background limited infrared photodetector (BLIP) limit. In this approximation the *NEP* is given by [1,2]

$$NEP = h\nu \left(\frac{2A\Phi_b\Delta f}{\eta} \right)^{1/2}, \quad (6)$$

where Φ_b is the total background photon flux density reaching the detector and Δf is the electrical bandwidth of the receiver. The background photon flux density received by the detector depends on its angular view of the background and on its ability to respond to the wavelengths contained in this source.

Typical D^* values for available optical detectors are shown in Figs. 1 and 2. Figure 1 shows the spectral detectivity of optical detectors responding in 0.1–1.2 μm region. Note that detectivity is not D^* , but rather reciprocal of *NEP* for a 1-Hz bandwidth. This figure of merit is employed to include photomultipliers whose noise does not depend in all cases upon the square root of the photocathode area. Table 3 lists the areas which Seib and Aukerman [3] state are proper to the various detectors illus-

trated. The reader can convert to the D^* values appropriate to the photoresistors and photovoltaic detectors by multiplying the detectivity value illustrated by the square root of the detector area. The signal fluctuation limit shown in the figure is independent of area [see Eq. (5)].

Table 2. Thermal detectors.

Detector	Method of operation
Bolometer Metal Semiconductor Superconductor Ferroelectric Hot electron	Change in electrical conductivity
Thermocouple/Thermopile	Voltage generation, caused by change in temperature of the junction of two dissimilar materials
Pyroelectric	Changes in spontaneous electrical polarization
Golay cell/Gas microphone	Thermal expansion of a gas

Table 3. Areas of detectors illustrated in Fig. 1.

Detector	Area (cm^2)
CdS photoconductor (PC)	1.00
CdSe photoconductor (PC)	1.00
Si Schottky barrier photodiode	0.03
Si p-n junction photodiode	0.25
Si photoconductor	0.25
Si avalanche photodiode	0.07
Ge photoconductor (PC)	0.20
Ge ac bias photoconductor (PC)	2.4×10^{-5}
Photomultipliers (PM)	1.00

For infrared focal plane arrays (FPAs), the relevant figure of merit is the noise equivalent temperature difference (*NEDT*). Noise equivalent difference temperature of a detector represents the temperature change, for incident radiation, that gives an output signal equal to the rms noise level. *NEDT* is defined

$$NEDT = \frac{V_n (\partial T / \partial Q)}{(\partial V_s / \partial Q)} = V_n \frac{\Delta T}{\Delta V_s}, \quad (7)$$

where V_n is the rms noise and ΔV_s is the signal measured for the temperature difference ΔT . It can be approximated that

$$NEDT = (C\eta_{BLIP}\sqrt{N_w})^{-1}, \quad (8)$$

where C is the thermal contrast, N_w is the number of photo-generated carriers integrated for one integration time, t_{int}

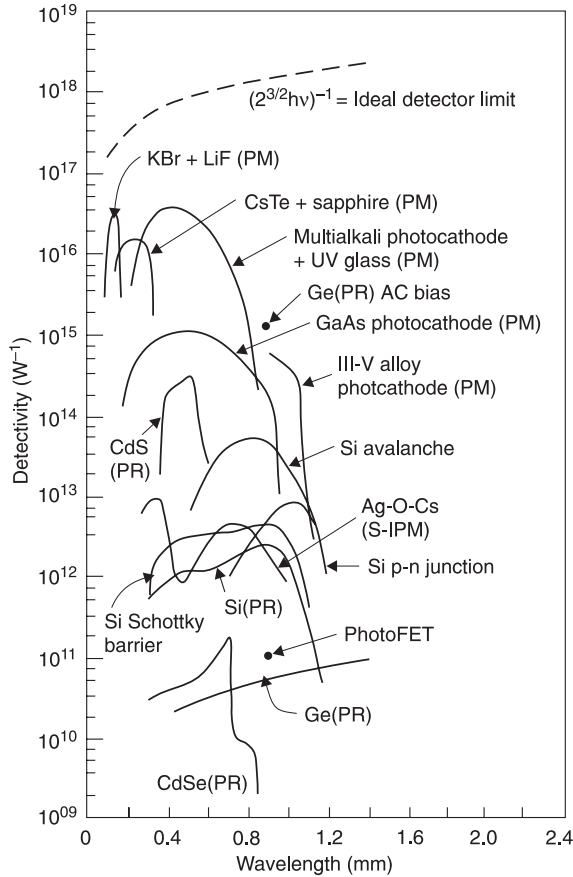


Fig. 1. Detectivity vs wavelength values of 0.1–1.2 μm photo-detectors. PR indicates a photoresistors and PM indicates a photo-multiplier. Detector areas are given in Table 2 (after Ref. 3).

$$N_w = \eta A t_{int} Q_B \quad (9)$$

where Q_B is the photon flux density incident on the detector area A .

Percentage of BLIP, η_{BLIP} , is simply the ratio of photon noise to composite FPA noise

$$\eta_{BLIP} = \left(\frac{N_{photon}^2}{N_{photon}^2 + N_{FPA}^2} \right)^{1/2} \quad (10)$$

It results from the above formulas that the charge handling capacity of the readout, the integration time linked to the frame time, and dark current of the sensitive material becomes the major issues of IR FPAs. The $NEDT$ is inversely proportional to the square root of the integrated charge and therefore the greater the charge, the higher the performance.

4. Focal plane array architectures

The term “focal plane array” (FPA) refers to an assemblage of individual detector picture elements (“pixels”) located at the focal plane of an imaging system. Although the definition could include one-dimensional (“linear”) arrays as well as two-dimensional (2D) arrays, it is frequently applied to the latter. Usually, the optics part of an optoelectronic images device is limited only to focusing of the image onto the detectors array. These so-called “staring arrays” are scanned electronically usually using circuits inte-

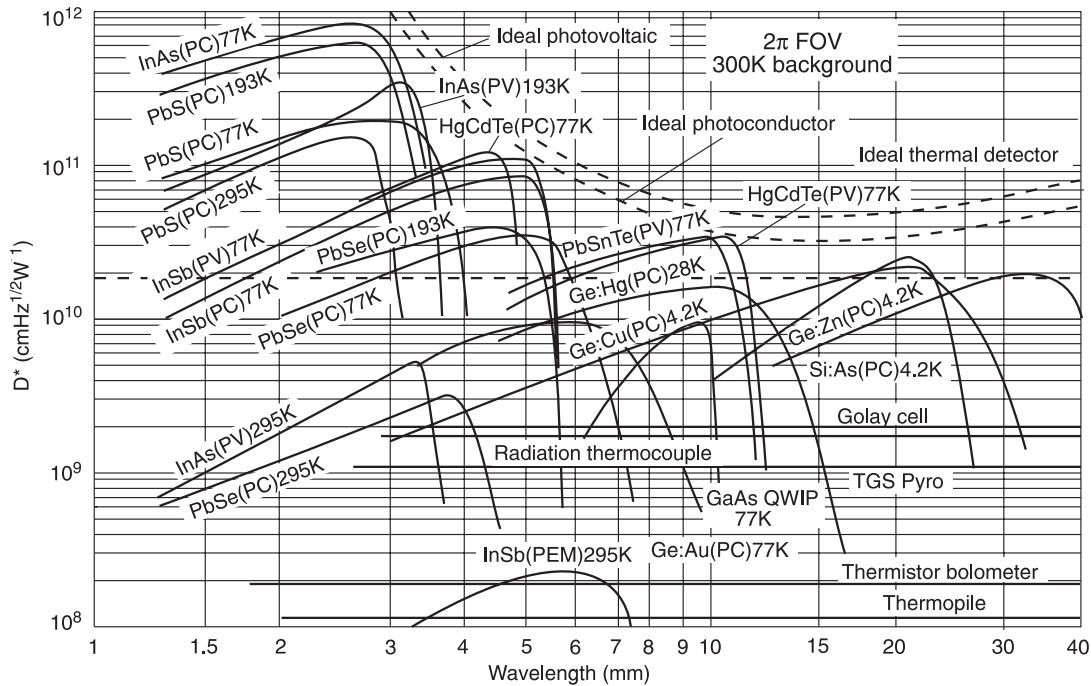


Fig. 2. Comparison of the D^* of various commercially available infrared detectors when operated at the indicated temperature. Chopping frequency is 1000 Hz for all detectors except the thermopile (10 Hz), thermocouple (10 Hz), thermistor bolometer (10 Hz), Golay cell (10 Hz) and pyroelectric detector (10 Hz). Each detector is assumed to view a hemispherical surround at a temperature of 300 K. Theoretical curves for the background-limited D^* for ideal photovoltaic (PV) detectors, photoresistors (PR) and thermal detectors are also shown.

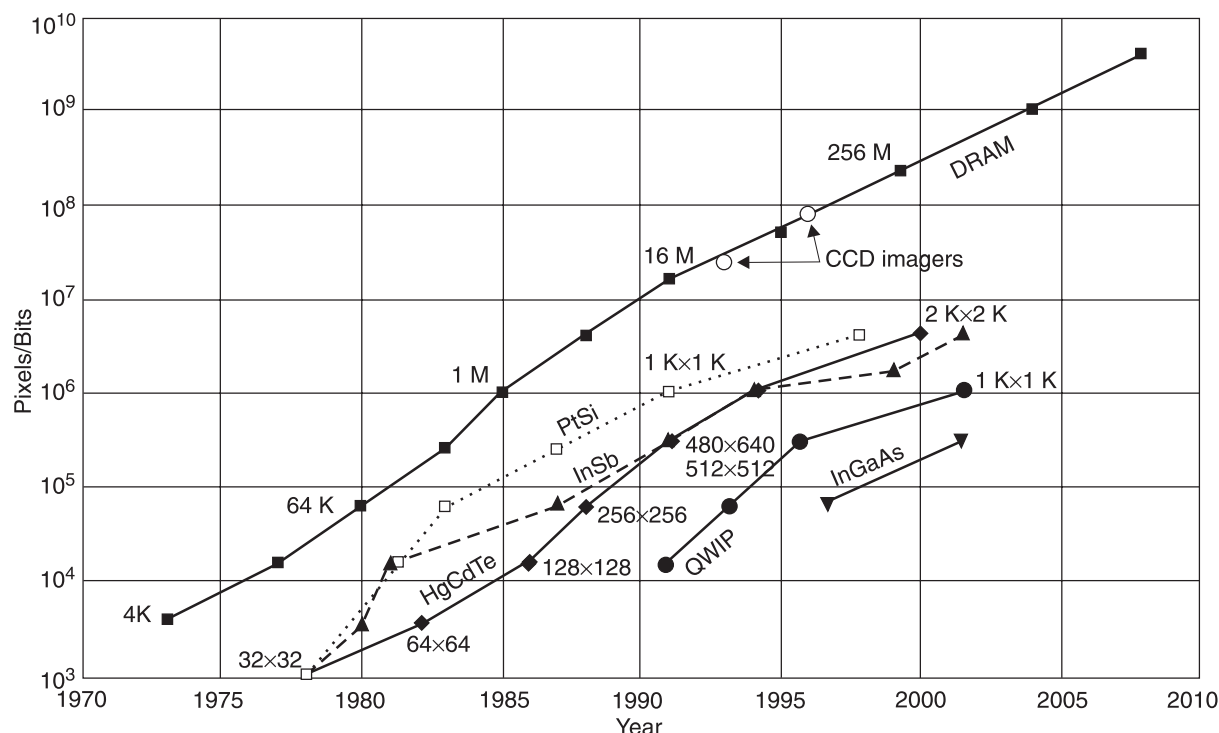


Fig. 3. Increase in array format size over the past thirty years (after Ref. 4).

grated with the arrays. The architecture of detector-readout assemblies has assumed a number of forms which are discussed below. The types of readout integrated circuits (ROICs) include the function of pixel deselecting, anti-blooming on each pixel, subframe imaging, output preamplifiers, and may include yet other functions. Infrared imaging systems, which use 2D arrays, belong to so-called "second generation" systems.

Development of detector FPA technology has revolutionized many kinds of imaging in the past twenty five years [4]. From γ rays to the infrared and even radio waves, the rate at which images can be acquired has increased by more than a factor of a million in many cases. Figure 3 illustrates the trend in array size over the past thirty years. Imaging FPAs have developed in proportion to the ability of silicon integrated circuit (ICs) technology to read and process the array signals, and with ability to display the resulting image. FPAs have nominally the same growth rate as dynamic random access memory (DRAM) ICs (which have had a doubling-rate period of approximately 18 months; it is a consequence of Moore's law, which predicts the ability to double transistor integration on each IC about every 18 months) but lag behind in size by about 5–10 years. ROICs are somewhat analogous to DRAM-only readouts, but require a minimum of three transistors per pixel, compared to one for each memory cell. Readouts are also analogous in terms of an emphasis on low noise inputs and generally maximum charge storage capacity. Charge coupled devices (CCDs) with close to 100 M pixels offer the largest formats. PtSi, InSb and HgCdTe have been following the pace of DRAM. In the infrared, 4 M pixel arrays are now available for astronomy applications.

4.1. Monolithic arrays

In general, the architectures of FPAs may be classified as monolithic and hybrid. When the detector material is either silicon or a silicon derivative (such as e.g. platinum silicide PtSi), the detector and ROIC can be built on a single wafer (see Fig. 4). Efforts to develop monolithic FPAs using narrow-gap semiconductors have failed. There are a few obvious advantages to this structure, principally in the simplicity and lower cost associated with a directly integrated structure. Common examples of these FPAs in the visible and near infrared (0.7–1.0 μm) are found in camcorders and digital cameras. Two generic types of silicon technology provide the bulk of devices in these markets: charge coupled devices (CCDs) and complementary metal-oxide-semiconductor (CMOS) imagers. CCD technology has achieved the highest pixel counts or largest formats with the numbers approaching 10^8 (see Fig. 5). CMOS imagers are also rapidly moving to large formats and are expected to compete with CCDs for the large format applications within a few years. Because the CCD imager market is much smaller than that for CMOS devices in general, it may be difficult for CCD to remain competitive in the long term.

CCD technology is very mature in respect to both the fabrication yield and the attainment of near-theoretical sensitivity. Figure 6 shows the schematic circuit for a typical CCD imager. The monolithic array is based on a metal-insulator-semiconductor (MIS) structure. Incident radiation generates electron-hole pairs in the depletion region of the MIS structure. The photogenerated carriers are first integrated in an electronic well at the pixel and subse-

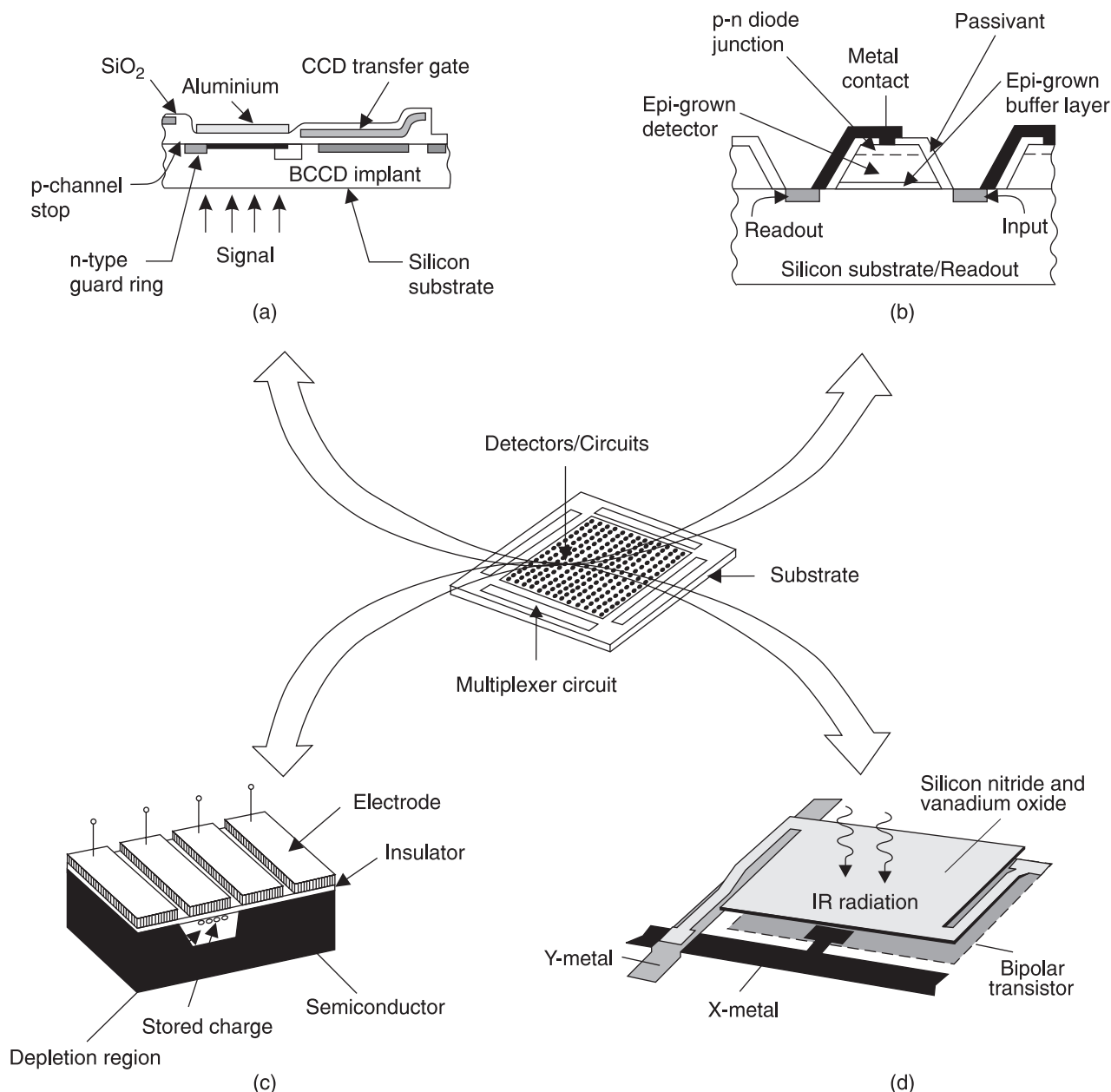


Fig. 4. Monolithic IR FPAs: (a) all-silicon; (b) heteroepitaxy-on-silicon; (c) non-silicon (e.g., HgCdTe CCD); and (d) microbolometer.

quently transferred to slow and fast CCD shift registers. This is done step by step as the gate biases are clocked to move the charge with minimal loss. The figure of merit for the effectiveness of this process is called the charge transfer efficiency (CTE). Channel stops between columns help to prevent charges from straying laterally. At the end of the CCD register, a charge carrying information on the received signal can be readout and converted into a useful signal.

The configuration of CCD devices requires specialized processing, unlike CMOS imagers which can be built on fabrication lines designed for commercial microprocessors. CMOS have the advantage that existing foundries, intended for application specific integrated circuits (ASICs), can be readily used by adapting their design rules. Design rules of

0.18 μm are in production, with pre-production runs of 0.13 μm design rules already underway. As a result of such fine design rules, more functionality has been put into the unit cells of multiplexers and smaller unit cells, leading to large array sizes. Figure 5 shows the timelines for minimum circuit features and the resulting CCD, IR FPA and CMOS visible imager sizes with respect to imaging pixels. Along the horizontal axis is also a scale depicting the general availability of various MOS and CMOS processes. The ongoing migration to even finer lithographies will thus enable the rapid development of CMOS-based imagers having even higher resolution, better image quality, higher levels of integration and lower overall imaging system cost than CCD-based solutions. At present, CMOS having with minimum features of $\leq 0.5 \mu\text{m}$ is also enabling monolithic

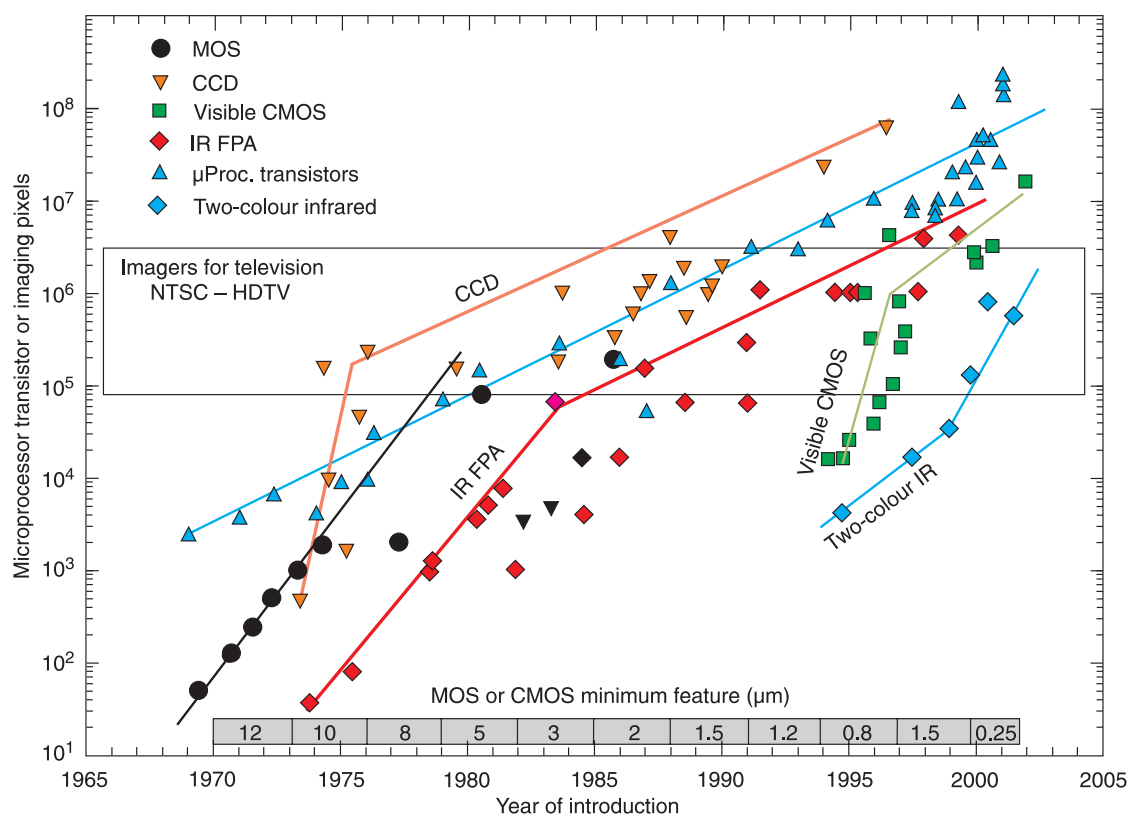


Fig. 5. Imaging array formats compared with the complexity of microprocessor technology as indicated by transistor count. The timeline design rule of MOS/CMOS features is shown at the bottom (after Ref. 4).

visible CMOS imagers, because the denser photolithography allows low-noise signal extraction and high performance detection with the optical fill factor within each pixel. The silicon wafer production infrastructure which has put personal computers into many homes is now enabling CMOS-based imaging in consumer products such as digital still and video cameras.

A typical CMOS multiplexer architecture (see Fig. 7) consists of fast (column) and slow (row) shift registers at the edges of the active area, and pixels are addressed one by one through the selection of a slow register, while the fast register scans through a column, and so on. Each photodiode is connected in parallel to a storage capacitor located in the unit cell. A column of diodes and storage ca-

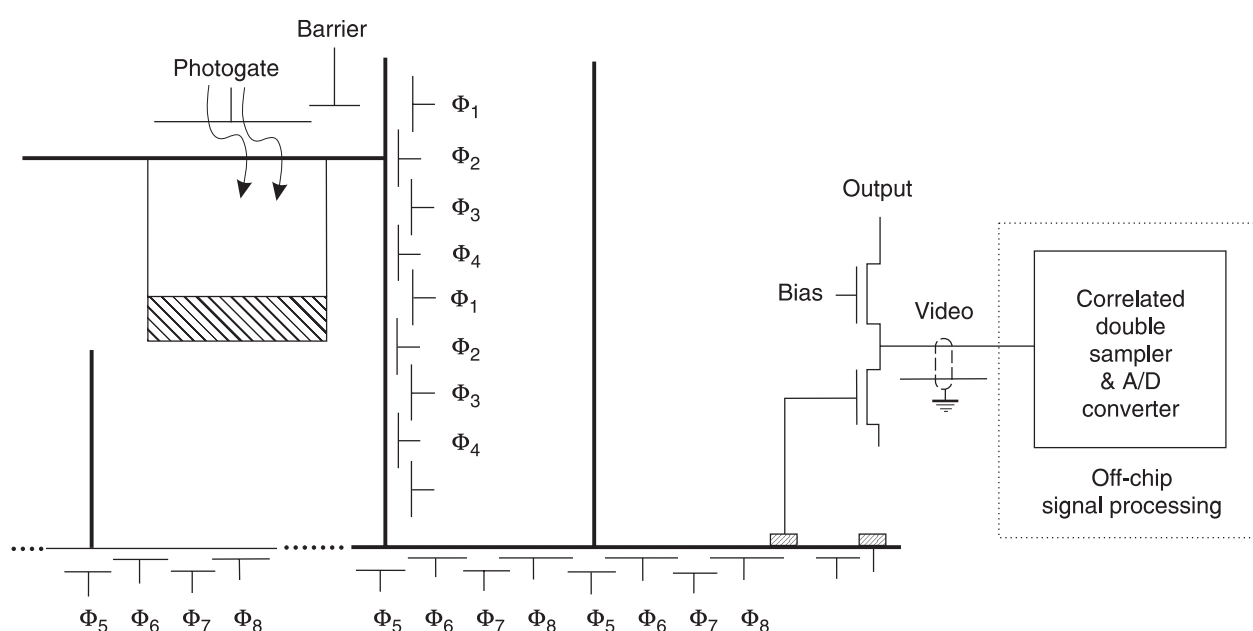


Fig. 6. Architecture of typical CCD imager (after Ref. 5).

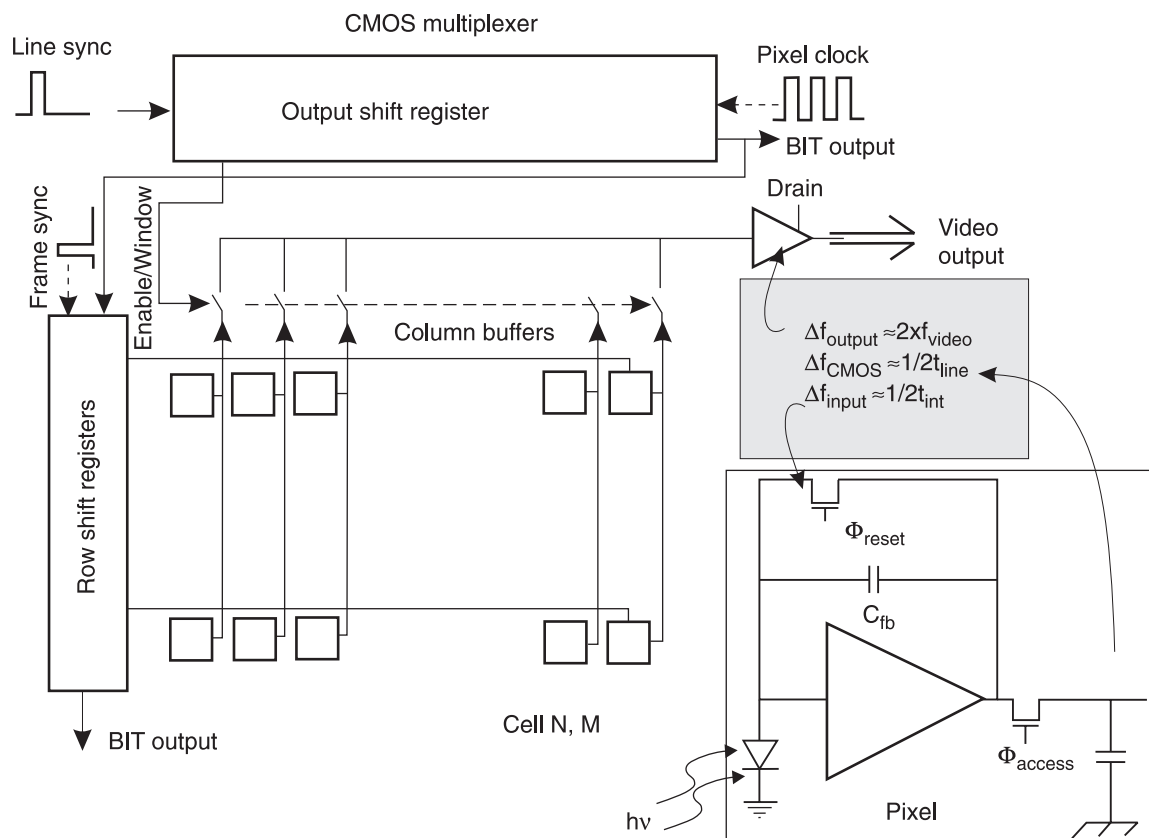


Fig. 7. CMOS multiplexing readout with CTIA detector interface (after Ref. 6).

pacitors is selected one at a time by a digital horizontal scan register and a row bus is selected by the vertical scan register. Therefore each pixel can be individually addressed.

CMOS-based imagers use active or passive pixels [6–8] as shown, in simplified form, in Fig. 8. In comparison with passive pixel sensors (PPSs), active pixel sensors (APSs) apart from read functions exploit some form of amplification at each pixel. PPSs have simple pixels consisting of as few as two components (a photodiode and a MOSFET switch). As a result, circuit overhead is low and the optical collection efficiency [fill factor (FF)] is high even for monolithic devices. A large optical FF of up to 80% maximises signal selection and minimises fabrication cost by obviating the need for microlenses. Microlenses, typically used in CCD and CMOS APS imagers for visible application, concentrate the incoming light into the photosensitive region when they are accurately deposited over each pixel (see Fig. 9). When the FF is low and microlenses are not used, the light falling elsewhere is either lost or, in some cases, creates artifacts in the imagery by generating electrical currents in the active circuitry.

APSs incorporate transistors in each pixel to convert the photogenerated charge to a voltage, amplify the signal voltage, and reduce the noise. Adding these components, however, reduces the FF of monolithic imagers to about 30–50% in 0.5- μm processes at a 5–6- μm pixel pitch or in 0.25- μm processes at a 3.3–4.0- μm pixel pitch [6].

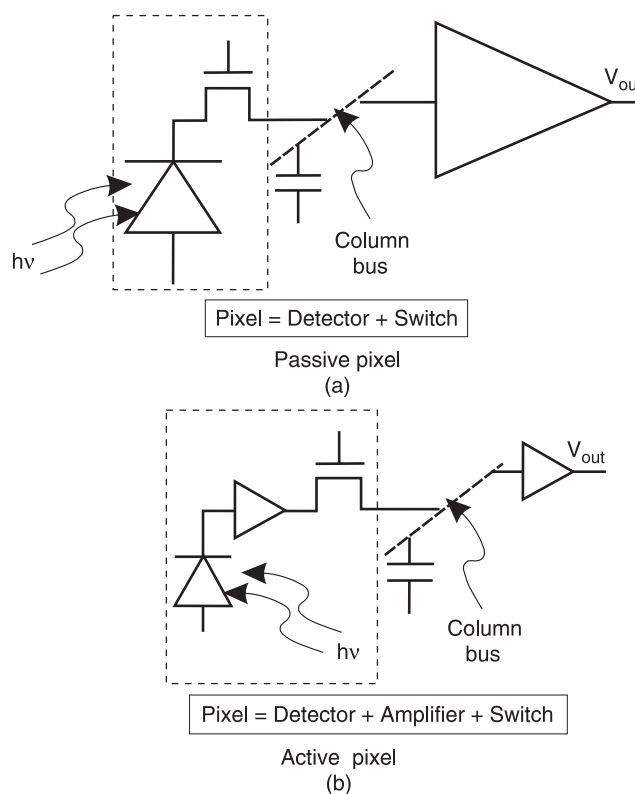
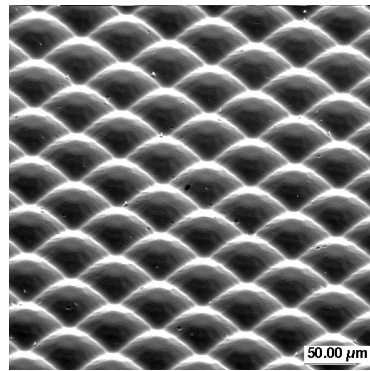


Fig. 8. Passive (a) and active (b) pixel sensor (after Ref. 6).



Micro-lens array

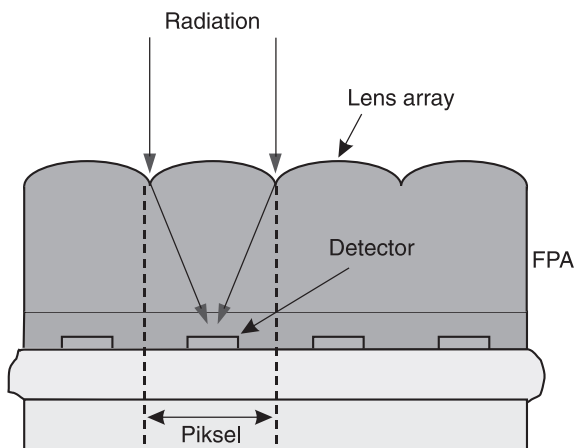


Fig. 9. Micrograph and cross-sectional drawing of microlensed hybrid FPAs (after Ref. 6).

4.2. Hybrid arrays

Ultraviolet and infrared imagers are most commonly built with a hybrid structure. Visible hybrids have also been built for specific applications. Hybrid FPAs detectors and multiplexers are fabricated on different substrates and mated with each other by flip-chip bonding or loop-hole interconnection (see Fig. 10). In this case, we can optimise the detector material and multiplexer independently. Other advantages of the hybrid FPAs are near 100% fill factor and increased signal-processing area on the multiplexer chip. Indium bump bonding of readout electronics, first demonstrated in the mid-1970s, provides for multiplexing the signals from thousands of pixels onto a few output lines, greatly simplifying the interface between the sensor and the system electronics.

The detector array can be illuminated from either the frontside (with the photons passing through the transparent silicon multiplexer) or backside (with photons passing through the transparent detector array substrate). In general, the latter approach is most advantageous as the multiplexer will typically have areas of metallizations and other opaque regions, which can reduce the effective optical area of the structure. When using opaque materials, substrates must be thinned to 10–20 μm in order to obtain sufficient quantum efficiencies and reduce the crosstalk.

Hybrids readouts are usually built with silicon, although a few demonstrations of readouts using other materials have been experimentally studied. Shift registers clock the signals from each row in turn, while all columns are typically read in parallel. The readout may have as few as

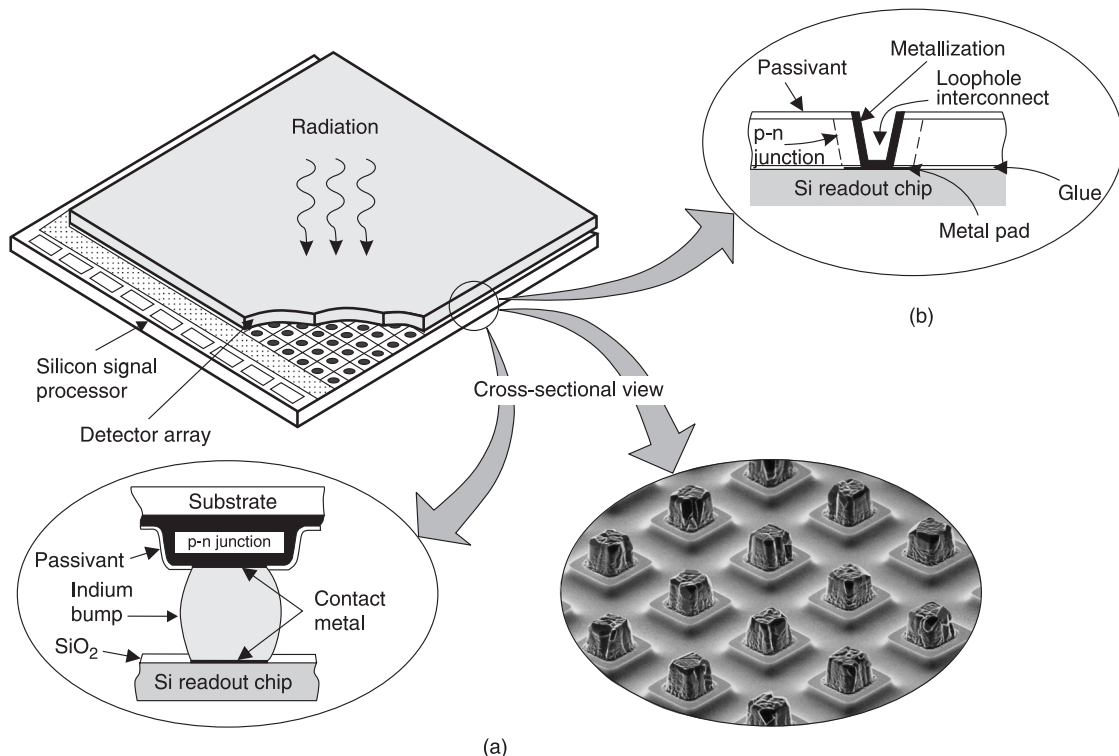


Fig. 10. Hybrid FPA with independently optimized signal detection and readout: (a) indium bump techniques, (b) loop-hole technique.

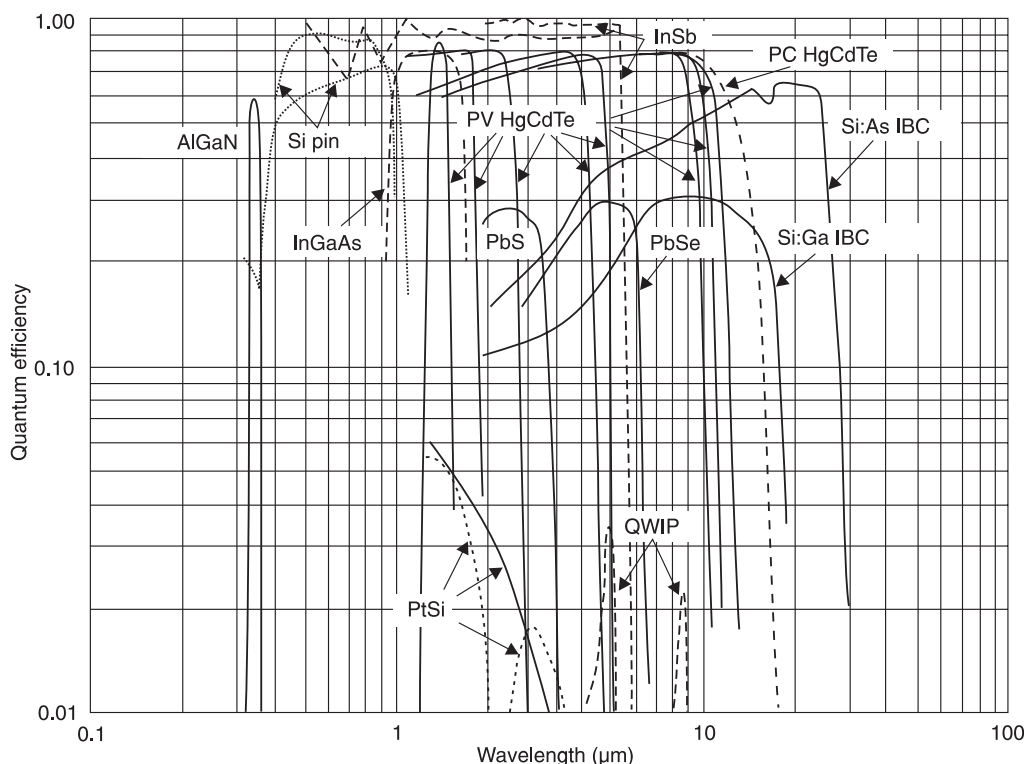


Fig. 11. Quantum efficiency of UV, visible, and infrared detector arrays (after Ref. 4).

one, and as many as 64 outputs, depending on the format size and frame rate. A typical output can provide 5–20 MHz data rates [4].

A wide variety of detector materials have been adapted to the monolithic and hybrid format [9–12]. Figure 11 shows the quantum efficiency of some of the detector materials used to fabricate arrays of ultraviolet (UV), visible and infrared detectors. AlGaAs detectors are being developed in the UV region. Silicon p-i-n diodes are shown with and without antireflection coating. Lead salts (PbS and PbSe) have intermediate quantum efficiencies, while PtSi Schottky barrier types and quantum well infrared photodetectors (QWIPs) have low values. InSb can respond from the near UV out to 5.5 μm at 80 K. A suitable detector material for near-IR (1.0–1.7- μm) spectral range is InGaAs lattice matched to the InP. Various HgCdTe alloys, in both photovoltaic and photoconductive configurations, cover from 0.7 μm to over 20 μm . Impurity-doped (Sb, As, and Ga) silicon impurity-blocked conduction (IBC) detectors operating at 10 K have a spectral response cut-off in the range of 16 to 30 μm . Impurity-doped Ge detectors can extend the response out to 100–200 μm .

UV, visible, and infrared arrays most commonly employ a photodiode structure. Photodiodes are preferred to photoconductors because of their relatively high impedance, which matches directly into the high input impedance stage of an FET readout circuit and also allows lower power dissipation. Mesa photodiodes are used in AlGaAs, InSb, and HgCdTe detectors, whereas planar photodiodes are used in Si, PtSi, Ge, HgCdTe, InGaAs, and InSb detectors. A third photodiode structure – used exclusively with

HgCdTe detectors – is the high-density vertically-integrated photodiode, or loop-hole photodiode [13].

Key to the development of ROICs has been the evolution in input preamplifier technology. This evolution has been driven by increased performance requirements and silicon processing technology improvements. A brief discussion of the various circuits is given in Ref. 14.

5. Optical focal plane arrays

Detector arrays are available in wide spectral range of electromagnetic spectrum. A variety of detector array formats are elaborated in the visible and infrared regions. Fewer options are available in the shorter or longer wavelength regions. Below we will survey a sample of the types that have been built to address the various portions of the optical spectrum.

5.1. X-ray detector arrays

In the course of the past hundred years the X-ray detection has migrated from film to digital cameras for dental and medical applications. Several classes of X-ray sensor arrays have been developed including [4]:

- phosphors,
- scintillators,
- microchannel plates,
- silicon detector arrays (CCDs, hybrid p-i-n structures, thin film silicon panels), and
- CdZnTe hybrid detector arrays.

5.1.1. Phosphors, scintillators, and microchannel plates

Phosphors absorb X-ray photons and emit visible photons as a result of returning of the excited electrons in the material to their ground state. Phosphors are generally used in a thin film layer of polycrystalline material and hence provide excellent spatial resolution, but absorb X-rays relatively weakly. Usually, phosphors were combined with photographic films, but today they can be combined with a visible detector array to improve an X-ray detective system.

Also scintillator crystals convert X-ray photons to visible light. To maximize the density of available electrons to interact with X-rays, large and optically transparent single crystals of high-Z materials are used. Examples include the alkali halide materials (NaI is doped with small amounts of Tl while CsI is doped with Na). They are typically 5-mm thick to absorb incident energies from 20 to 100 keV with conversion efficiency (the fraction of X-ray energy converted to visible light) around 10%. Scintillators are combined with a visible detector array.

The microchannel plate (MCP) is a disk consisting of millions of micro glass tubes (channels) fused in parallel with each other. The channels made of combination of oxides of silicon, lead, and alkali compounds in mixture are used to obtain design resistivity in the approximate range of 10^{10} – $10^{15} \Omega \text{ cm}^2$. Each channel acts as an independent electron multiplier. Its diameter is typically 10 μm and length of 0.5 mm and then is possible incorporate 3 million of them in a 25 mm plate. They are operated at approximately 1 kV with a typical amplification of 3000. The electron gain of the channel depends on the applied voltage, the ratio of the channel length to the diameter and the secondary emission characteristics of the channel surface. The gain up to 10^8 for 3 keV applied field is achieved. Quantum efficiency can vary considerably from as low as 1% to as high as 60%. It depends upon energy, angle of incidence, and coating of the channel walls and channel entrance. The MCP offers faster time response; temporal resolution is

10^{-10} s under favourable conditions. It also features good immunity from magnetic fields and 2D detection ability when multiple anodes are used.

MCP arrays are used in the UV and visible spectral regions as well as for X-rays. An X-ray-sensitive MCP is illustrated in Fig. 12, which is used in the high-resolution camera on board the Advanced X-ray Astrophysics Facility (AXAF) satellite renamed Chandra after its 1999 launch. As we can see, two MCP stages amplify the electron stream which is collected by a crossed grid of wires connected to charge-sensitive amplifiers.

5.1.2. Silicon detector arrays

Between different silicon detector arrays in the X-ray region, the most important are charge-coupled devices (they are discussed in greater detail in section 5.3). For example, Fig. 13 shows the advanced CCD imaging spectrometer (ACIS) used for studying the temperature variation across X-ray sources such as vast clouds of hot gas in intergalactic space.

CCD detectors are susceptible to radiation damage and failure when operated for extended periods in space environments. The main reason of that is CCD surface inversion from accumulated surface charge build up. It appears that hybrid structures with readouts compatible with silicon p-i-n diodes can be hardened to very high radiation dosages, and the p-i-n device itself is also quite resistant to radiation damage [4].

Figure 14 shows silicon p-i-n diodes fabricated in a lightly doped silicon wafer with a common back electrode and an array of the opposite doping type on the front side. Metal contacts are made to the front-side p⁺-doped regions. These devices give relatively good energy resolution since the total thickness of the i-region is fully depleted and all the absorbed charge in the active region is efficiently collected.

Thin-film silicon panels are usually used for medical imaging when a very large area and high-resolution arrays

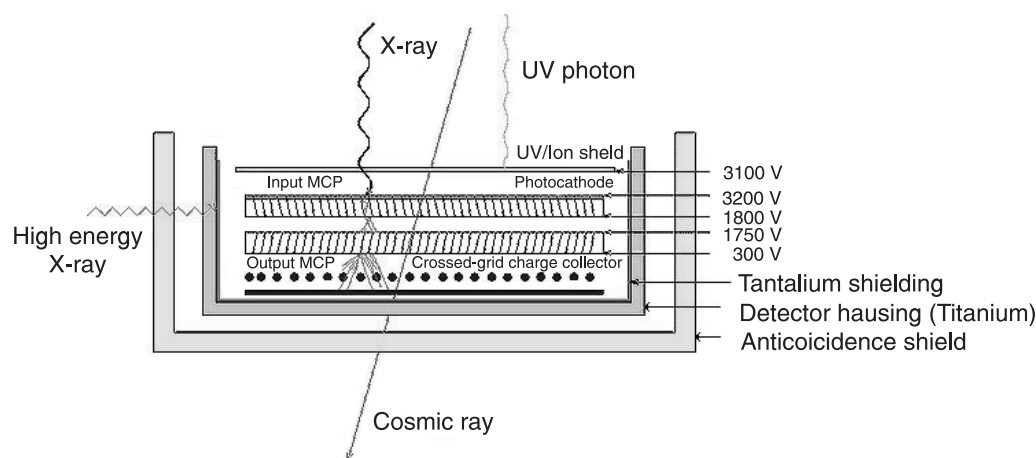


Fig. 12. Diagram of MCP detector in the high resolution camera (HRC) on the Advanced X-ray Astrophysics Facility (AXAF) satellite renamed Chandra (after Ref. 15).

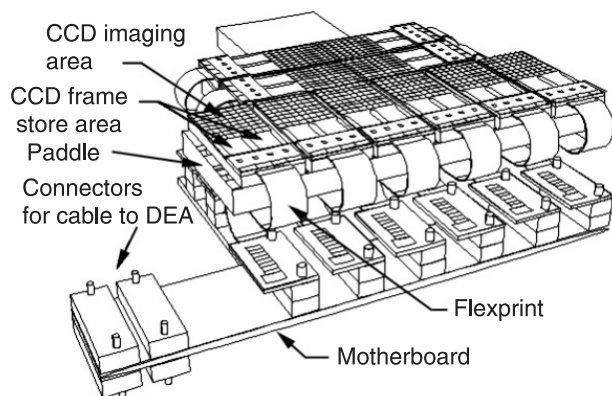


Fig. 13. A diagram of the Chandra advanced CCD imaging spectrometer (ACIS) (after Ref. 16).

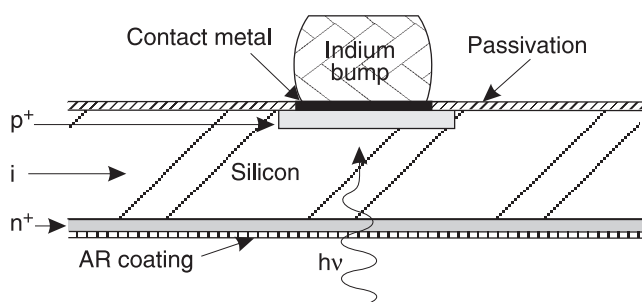


Fig. 14. Silicon p-i-n diode array used in hybrid X-ray detector arrays.

are needed. As an active material, the thin-film of amorphous silicon is deposited on a substrate using chemical vapour deposition (CVD) method. Each pixel of the array, photolithographically processed, consists of a photodiode and an addressable switch to read out the photocurrent. To convert incident X-rays to visible light, a scintillating material such as $\text{Gd}_2\text{O}_2\text{S:Tb}$ is deposited in proximity over the amorphous silicon array. Figure 15 shows X-ray image of a female hand taken with this panel. Typical X-ray sensitivity converts the 40- to 150-keV range.

5.1.3. CdZnTe hybrid arrays

CdZnTe has become established as perhaps the most suitable material for the detection of X-rays and gamma-rays. Discrete detectors and arrays fabricated from $\text{Cd}_{1-x}\text{Zn}_x\text{Te}$ (where $x = 0.08\text{--}0.3$) are becoming more widely used to detect nuclear radiation in medicine, industry and scientific research. Devices fabricated from the most common detector material, germanium, offer high resolution but require liquid nitrogen cooling. Although NaI(Tl) scintillators do not require cooling, they suffer from low resolution compared to CdZnTe, and they are bulky. NaI(Tl) relies on secondary detection; photons hit the scintillator, producing light, which is in turn detected by a visible detector array. In contrast, photons reaching the CdZnTe detector are directly converted into an electrical signal, which is then am-



Fig. 15. X-ray image of a female hand taken with a thin-film silicon array. The active panel covers $28.2 \times 40.6 \text{ cm}^2$ and has over 7.1 megapixels (2232×3200 pixels) on $127\text{-}\mu\text{m}$ centres with a fill factor of 57%. Exposure may last up to 6 sec with the standard electronics (after Refs. 4 and 17).

plified by standard electronic circuitry. The relatively high density (5.78 g/cm^3) of CdZnTe provides good absorption efficiency. The higher resistivity of CdZnTe (around $3 \times 10^{10} \Omega \text{ cm}$) results in low leakage currents in photovoltaic devices (MSM devices and p-n junctions), and also allows the use of higher bias voltage. In turn, this improves the charge-collection efficiency and allows the fabrication of large volume detectors. Large CdZnTe crystals are grown using modified standard or vertical furnaces by the high pressure of inert gas inside the crucible [18,19]. Large crystals are also used in fabrication of hybrid focal plane arrays [20].

An example of a CdZnTe X-ray detector structure is shown in Fig. 16. As an active material, lightly doped,

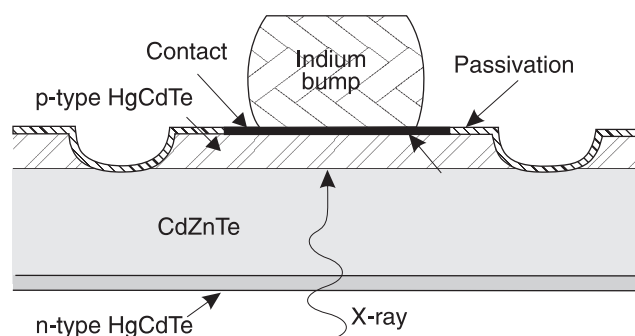


Fig. 16. CdZnTe diode array (after Ref. 4).

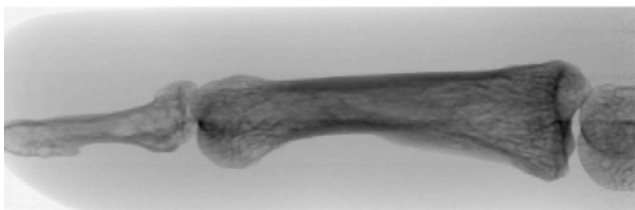


Fig. 17. Digital X-ray image of an index finger taken with a CdZnTe array (192×340 pixels with 50- μ m size) (after Ref. 4).

high-resistivity material is used. To solve the problem of forming ohmic contacts to CdZnTe wide-band gap material, the narrower-band-gap both p- and n-type HgCdTe epitaxial layers are used. The pixel size is typically 50 μ m what has influence on high spatial image resolution (see Fig. 17). Such arrays can yield very high quality, digital X-ray images of small objects.

5.2. Ultraviolet detector arrays

Ultraviolet (UV) imagers are most commonly built with a hybrid structure. An example is $\text{Al}_x\text{Ga}_{1-x}\text{N}$ (AlGaN) material sensitive to UV radiation while being insensitive to longer wavelength radiation [21–23]. Such devices have applications where there is a need to detect or control the source of UV radiation in an existing background of visible or infrared radiation. Examples of such applications include flame detection, furnace and engine monitoring for the automotive, aerospace and petroleum industry, undersea communications, UV astronomy, space-to-space communications secure from the Earth, early missile threat warning and airborne UV countermeasures, and portable battlefield reagent/chemical analysis system. Because of their theoretical intrinsic solar blindness and low dark currents, III-Nitride based devices are expected to work without optical filters and complex electronics, thus

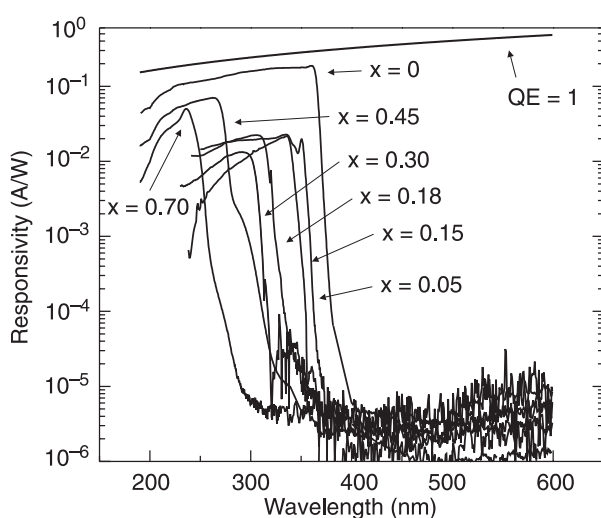


Fig. 18. Responsivity of $\text{Al}_x\text{Ga}_{1-x}\text{N}$ p-i-n photodiodes showing a cut-off wavelength continuously tunable from 227 to 365 nm, corresponding to an Al concentration in the range 0–70% (after Ref. 24).

significantly reducing the launch weight for space and airborne applications. The goal of this development is to achieve “solar blind” spectral response of 280 nm because ozone in the atmosphere absorbs nearly all sunlight shorter than this wavelength.

Most of the research on UV photodetectors has been recently directed toward the demonstration of AlGaN based p-i-n junction photodiodes, which present the capability of tailoring the cut-off wavelength by controlling the alloy composition and thus, the bandgap energy of the active layer. A full range of $\text{Al}_x\text{Ga}_{1-x}\text{N}$ p-i-n photodiodes has been demonstrated with a cut-off wavelength continuously tunable from 227 to 365 nm, corresponding to an Al concentration in the range of 0–70%. This can be seen in Fig. 18 where the current responsivity of these detectors at room temperature is shown. Their internal quantum efficiencies were up to 86% when operated in photovoltaic mode (i.e. at zero bias) and they exhibited an UV-to-visible rejection ratio as high as six orders of magnitude. In addition to these front-side illuminated devices, backside illuminated AlGaN UV photodiodes have also recently been reported using sapphire substrates, which are UV transparent. Sapphire has only a moderate thermal coefficient of expansion mismatch with silicon readouts.

The successful development of large-format UV imaging arrays consisting of 320×256 p-i-n photodiodes has been reported by Longo *et al.* [25]. Figure 19 shows a visi-



(a)



(b)

Fig. 19. Engineering Graduate Research on the North Carolina State University campus: (a) visible image, (b) UV image (after Ref. 25).

ble image of university campus and below, the corresponding image obtained using 320×256 visible blind FPAs.

5.3. Visible detector arrays

Silicon photodiodes are widely applied in spectral range below 1.1 μm and even are used for X-ray and gamma ray detectors. The main types are as followed:

- p-n junctions generally formed by diffusion (ion implantation is also used),
- p-i-n junctions (because of thicker active region, they have enhanced near-IR spectral response),
- UV- and blue-enhanced photodiodes, and
- avalanche photodiodes.

Typical spectral characteristics of planar diffusion photodiodes are shown in Fig. 20. The time constant of p-n junction silicon photodiodes is generally limited by RC constant rather than by the inherent speed of the detection mechanism (drift and/or diffusion) and is on the order of microsecond. Detectivity is typically between mid- 10^{12} to 10^{13} $\text{cmHz}^{1/2}/\text{W}$ usually amplifier-limited for small area detectors.

The p-i-n detector is faster but is also less sensitive than conventional p-n junction detector and has slightly ex-

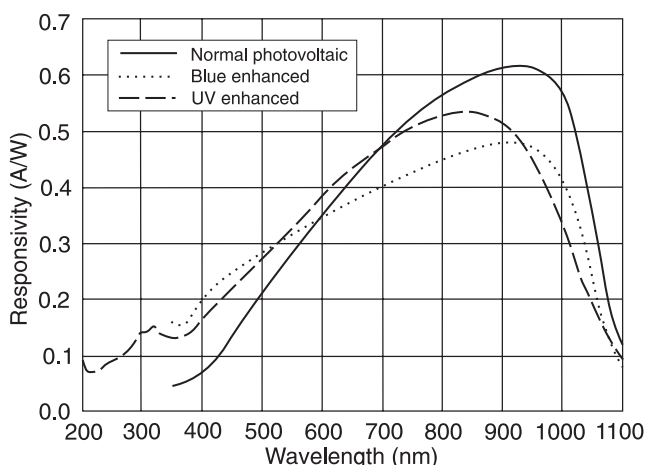


Fig. 20. Typical current responsivity of several different types of planar diffused silicon photodiodes (after Ref. 26).

tended red response. It is a consequence of extension of the depletion layer width, since longer wavelength photons will be absorbed in the active device region. Incorporation of a very lightly doped region between the p and n regions and a modest reverse bias form a depletion region the full thickness of the material ($\approx 500 \mu\text{m}$ for a typical silicon wafer). Higher dark current collected from generation within the wider depletion layer results in lower sensitivity.

High absorption coefficient of silicon in the blue and UV spectral regions causes generation of carriers within the heavily doped p^+ (or n^+) contact surface of p-n and p-i-n photodiodes, where the lifetime is short due to the high and/or surface recombination. As a result, the quantum efficiency degrades rapidly in these regions. Blue- and UV-enhanced photodiodes optimize the response at short wavelengths by minimizing near-surface carrier recombination. This is achieved by using very thin and highly graded p^+ (or n^+ or metal Schottky) contacts, by using lateral collection to minimize the percentage of the surface area which is heavily doped, and/or passivating the surface with a fixed surface charge to repel minority carriers from the surface.

The avalanche photodiodes are especially useful where both fast response and high sensitivity are required. An optimum gain exists below which system is limited by receiver noise and above which shot noise dominates receiver noise and the overall noise increases faster than the signal. Noise is a function of detector area and increases as gain increases. Typical detectivity is $(3-5) \times 10^{14}$ $\text{cmHz}^{1/2}/\text{W}$.

Monolithic imaging FPAs for the visible spectrum began in the early 1960s. Further development is shown in Fig. 5. At present, two monolithic technologies provide the bulk of devices in the markets of camcorders and digital cameras: CCD and CMOS imagers. The fundamental performance parameters common to both CCD and CMOS imagers has been recently compared by Janesick [27,28]. Compared to CCD, CMOS performance is currently preventing the technology from scientific and high end use. Custom CMOS pixel designs and fabrication process are required to improve performance.

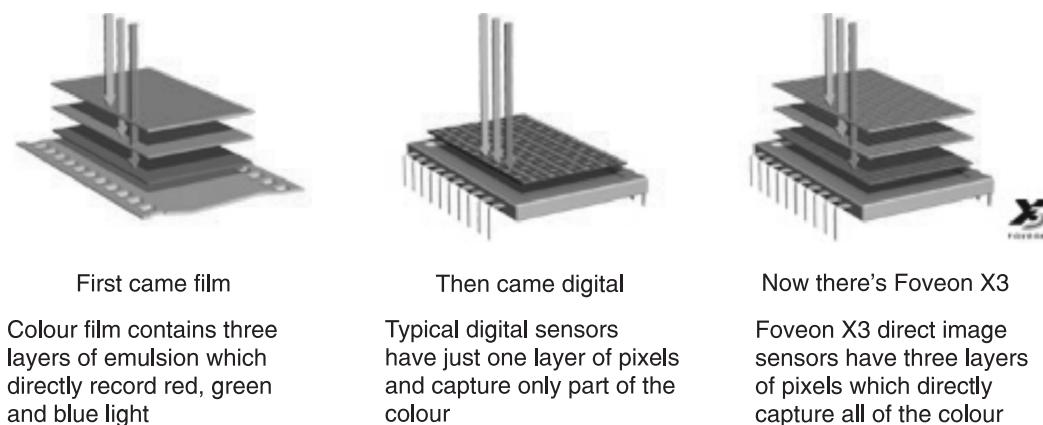


Fig. 21. Evolution in design of colour pixels (after Ref. 29).

The colour film has traditionally been held as the gold standard for photography. It produces rich, warm tones and incredible colour detail that consumers around the world have become accustomed to. Film has achieved this by using three layers of emulsion to capture full colour at every point in the image.

Digital CCD image sensors were developed approximately 30 years ago, ushering in the era of digital photography. In visible imaging, CCD arrays integrate the readout and sensor in a combined pixel and integrated red-green-blue (RGB) colour filters are included (see Fig. 21). The most common checkerboard filter pattern dedicates 2 out of 4 pixels to green, and 1 pixel each to red and blue. As a result, the sensor gathers only 50% of the green light and 25% of the red and blue. Digital post-processing interpolates to fill in the blanks, so more than half of the image is artificially generated and innately imperfect. In this case the fill factor is only a fraction of the pixel area; e.g. about 70% for 16.6-megapixel CCD array from Kodak [30]. Unfortunately, the rich, warm tones and detail of colour film that the world came to expect suffered over the convenience and immediacy of digital. This was due to the fact that CCD digital image sensors were only capable of recording just one colour at each point in the captured image instead of the full range of colours at each location.

Foveon has combined the best of what both film and digital have to offer [31]. This is accomplished by the innovative design of Foveon's X3 direct image sensors which have three layers of pixels, just like film has three layers of chemical emulsion (see Fig. 21). Foveon's layers are embedded in silicon to take advantage of the fact that red, green, and blue light penetrate silicon to different depths (the photodetectors sensitive to blue light are on the top, the green-sensitive detectors are in the middle, and the red on the bottom) – forming the image sensor that captures full colour at every point in the captured image. This is 100% full-colour with no interpolation. For example, Fig. 22 illustrates a photograph taken with a three-chip Foveon CMOS camera.



Fig. 22. The Foveon studio camera uses three 10-megapixel chips to capture pictures that rival the quality of film cameras (after Ref. 32).

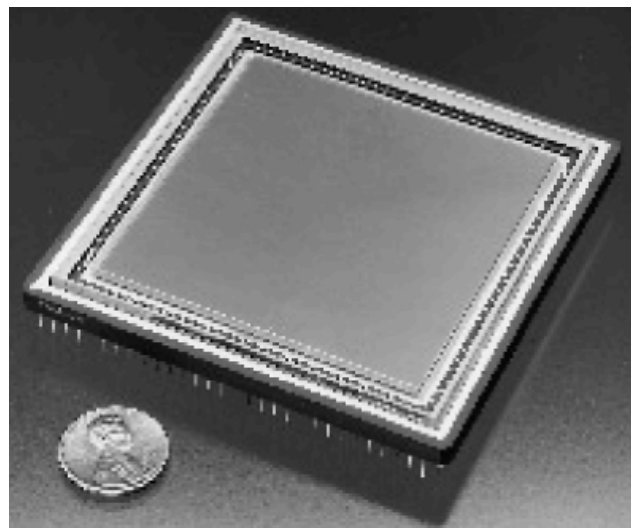


Fig. 23. Silicon CCD visible array with 5040×5040 pixels. Pixel size is 12×12 μm^2 . The chip size is 60×60 mm^2 . Quantum efficiency is > 20% at 900 nm (after Ref. 33).

The largest CCD colour arrays have approximately 25 megapixels. The array made by Dalsa can operate at 2.5 frames per second with eight outputs (see Fig. 23) and variations of this design have been made for a variety of imaging applications [4,33]. Pixel size is 12 μm . The chip size is over 60 mm on a side. For comparison, the chip size of 16.6 megapixel CMOS array from Foveon is considerably smaller – 22 mm on side, because the pixel size is only 4.5 μm . Quantum efficiency of the CMOS detectors is in the range of 30%.

Visible hybrids have also been built for special applications to take advantage of the materials flexibility and larger surface area with nearly 100% fill factor. Recently, Si p-i-n detector arrays for the astronomy and civil space communities in hybrid configuration with the size as large as 1024×1024 have been demonstrated [34]. Such structures features low capacitance diodes of 1 fF for an 18 μm pixels, which helps to minimize readout noise.

5.4. Infrared detector arrays

Although efforts have been made to develop monolithic structures using a variety of infrared detector materials (including narrow-gap semiconductors) over the past 30 years, only a few have matured to a level of practical use. These included PtSi, and more recently PbS, PbTe, and uncooled silicon microbolometers. Other infrared material systems (InGaAs, InSb, HgCdTe, GaAs/AlGaAs QWIP, and extrinsic silicon) are used in hybrid configurations.

5.4.1. InGaAs arrays

The need for high-speed, low-noise $\text{In}_x\text{Ga}_{1-x}\text{As}$ (InGaAs) photodetectors for use in lightwave communication systems operating in the 1–1.7 μm wavelength region ($x =$

0.53) is well established. $\text{In}_{0.53}\text{Ga}_{0.47}\text{As}$ alloy is lattice matched to the InP substrate. Having lower dark current and noise than indirect-bandgap germanium, the competing near-IR material, the material is addressing both entrenched applications including low light level night vision and new applications such as remote sensing, eye-safe range finding and process control. By changing the alloy composition of the InGaAs absorption layer, the photodetector responsivity can be maximized at the desired wavelength of the end user to enhance the signal to noise ratio.

InGaAs-detector processing technology is similar to that used with silicon, but the detector fabrication is different. The InGaAs detector's active material is deposited onto a substrate using chloride VPE or MOCVD techniques adjusted for thickness, background doping, and other requirements. Planar technology evolved from the older mesa technology and at present is widely used due to its simple structure and processing as well as the high reliability and low cost. InGaAs has also been grown on GaAs substrates to give better performance when the spectral cutoff is extended to $2.5\text{ }\mu\text{m}$ [35].

Both p-i-n and avalanche InGaAs photodiode structures with the total layer thicknesses of $4\text{--}7\text{ }\mu\text{m}$ are fabricated. In comparison to APDs operating in the same wavelength region, p-i-n photodiodes offer the advantages of lower dark current, larger frequency bandwidth, and simpler driving circuitry. Thus, although p-i-n diodes do not have internal gain, an optimal combination of a p-i-n diode with a low-noise, large-bandwidth transistor has led to high sensitivity optical receivers operating up to 2.5 Gb/s . For commercially available InGaAs/InP APDs, it is fairly difficult to respond reliably to 10 Gb/s range signals with moderate multiplication gain, due to their limited gain-bandwidth (BG) products. The GB products in these APDs are typically $20\text{ to }40\text{ GHz}$.

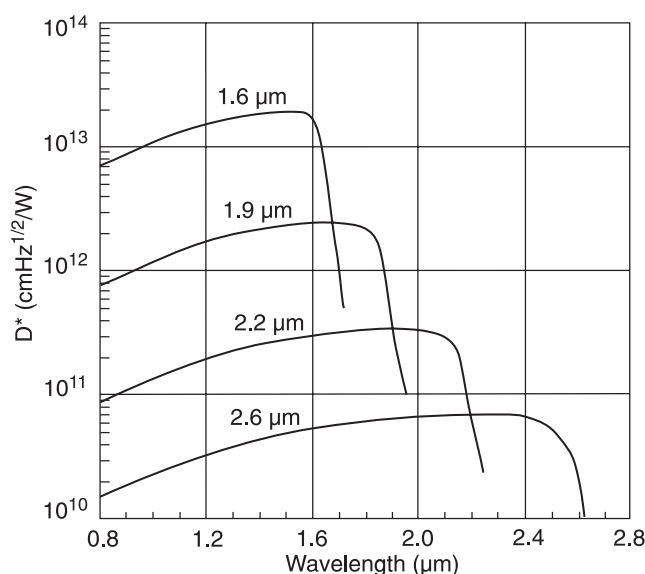


Fig. 24. Room temperature detectivity of InGaAs photodiodes with cutoff wavelength at $1.6\text{ }\mu\text{m}$, $1.9\text{ }\mu\text{m}$, $2.2\text{ }\mu\text{m}$, and $2.6\text{ }\mu\text{m}$, respectively.

Standard $\text{In}_{0.53}\text{Ga}_{0.47}\text{As}$ photodiodes have detector-limited room temperature detectivity of $\sim 10^{13}\text{ cmHz}^{1/2}\text{W}^{-1}$. With increasing cutoff wavelength, detectivity decreases. Figure 24 shows the spectral response of three such InGaAs detectors at room temperature, whose peak responsivity is optimized at $1.7\text{ }\mu\text{m}$, $2.0\text{ }\mu\text{m}$, and $2.4\text{ }\mu\text{m}$, respectively.

The largest and finest pitched imager in $\text{In}_{0.53}\text{Ga}_{0.47}\text{As}$ material system has been demonstrated recently [36]. The 640×512 FPAs with $25\text{-}\mu\text{m}$ pixels is sensitive to the $0.9\text{--}1.7\text{-}\mu\text{m}$ and features a room temperature detectivity greater than $5\times 10^{12}\text{ cmHz}^{1/2}/\text{W}$ with greater than 98% of the pixel operable.

5.4.2. Schottky-barrier photoemissive arrays

In 1973, Shepherd and Yang of Rome Air Development Center proposed the concept of silicide Schottky-barrier detector FPAs as much more reproducible alternative to HgCdTe FPAs for IR thermal imaging [37]. Since then, the development of the Schottky-barrier technology progressed continuously and has been commercialized for about 15 years, and both monolithic and hybrid versions have been produced.

The most popular Schottky-barrier detector is the PtSi detector, which can be used for the detection in the $3\text{--}5\text{ }\mu\text{m}$ spectral range. Figure 25 shows the basic construction and operation of the PtSi detector integrated with a silicon CCD. It is typically operated in backside illumination mode. Radiation is transmitted through the p-type silicon and is absorbed in the metal PtSi (not in the semiconductor), producing hot holes which are then emitted over the potential barrier into the silicon, leaving the silicide

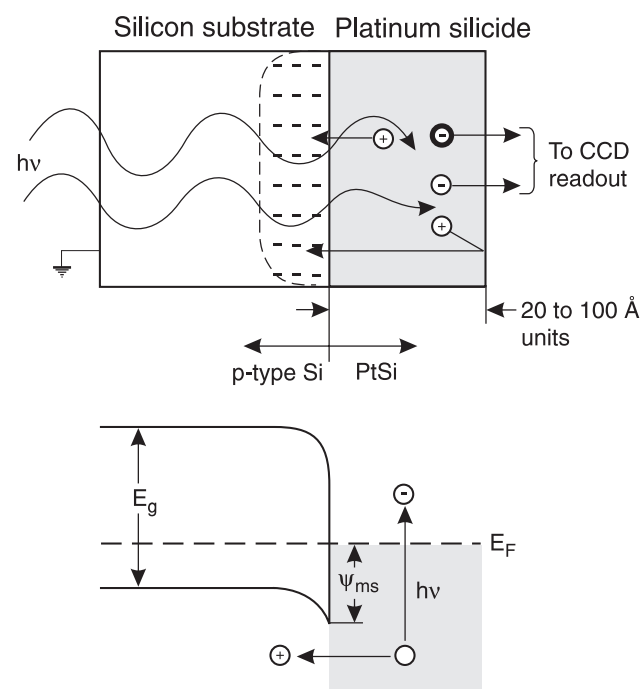


Fig. 25. Operation of PtSi/p-Si Schottky-barrier detector (after Ref. 38).

charged negatively. Negative charge of silicide is transferred to a CCD by the direct charge injection method.

For improving the monolithic array performance, Kimata and co-workers from Mitsubishi Corporation have developed a readout architecture called the charge sweep device (CSD) used in series of IR image sensors with array sizes up to 1040×1040 elements [39]. Although PtSi detectors has quite low quantum efficiency in the $3\text{--}5\text{ }\mu\text{m}$ atmospheric window (of the order of 1%), but excellent imagery of objects at room temperature (with temperature resolution as low as 0.033 K for 512×512 arrays) is obtained by means of near full frame integration in area arrays. At present however, the performance of monolithic PtSi Schottky-barrier FPAs has reached a plateau, and a slow progress from now on is expected [40,41].

5.4.3. Lead salt arrays

Lead salt thin film photoconductors were first produced in Germany and next in the United States at Northwestern University in 1944 and, in 1945, at the Admiralty Research Laboratory in England [42]. After 60 years, low-cost, versatile PbS and PbSe polycrystalline thin films remain the photoconductive detectors of choice for many applications in the $1\text{--}3\text{ }\mu\text{m}$ and $3\text{--}5\text{ }\mu\text{m}$ spectral range.

Lead salt chalcogenides are deposited on silicon or silicon oxide from wet chemical baths, or are grown epitaxially (usually using MBE technique) on silicon through the use of suitable buffer layers (usually $\text{CaF}_2\text{--BaF}_2$ layers) to overcome large thermal mismatch problems between silicon readout substrates and lead salt detectors [43]. Such monolithic solution avoids the use of a thick slab of these materials mated to silicon, as is done with typical hybrids. In the case of using chemical deposition, the detector material is deposited from a wet chemical solution to form polycrystalline photoconductive islands on CMOS multiplexer. Northrop Grumman elaborated monolithic PbS FPAs in a 320×240 format with pixel size of $30\text{ }\mu\text{m}$ [44].

The research group at the Swiss Federal Institute of Technology has demonstrated the first realization of monolithic PbTe FPA (96×128) on a Si-substrate containing the active addressing electronics [45].

5.4.4. InSb arrays

InSb photodiodes have been available since the late fifties last century and are generally fabricated by impurity diffusion and ion implantation. They are used in the $1\text{--}5\text{ }\mu\text{m}$ spectral region and must be cooled to approximately 77 K. InSb photodiodes can also be operated in the temperature range above 77 K. The quantum efficiency optimized for this temperature range remains unaffected up to 160 K [46].

In InSb photodiode fabrication, epitaxy is not used; instead, the standard manufacturing technique begins with bulk n-type single crystal wafers with donor concentration about 10^{15} cm^{-3} . Relatively large bulk grown crystals with

2-in. and 3-in. diameters are available on the market. An array hybrid size up to 2052×2052 is possible because the InSb detector material is thinned to less than $10\text{ }\mu\text{m}$ (after surface passivation and hybridization to a readout chip) which allows it to accommodate the InSb/silicon thermal mismatch. Recently, also growing of InSb and related alloys by MBE together with doping of substrate to induce transparency has been demonstrated. In the last case the thinning of the detector material is not required.

The largest hybrid arrays have been principally built for astronomy where dark currents as low as 0.01 electrons/sec are measured at 30 K [34]. The most recent development is the $2 \times 2\text{ K}$ format ($25\text{ }\mu\text{m}$ pixels). This array is nearly 55 mm on a side. Individual arrays can be arranged in groups to give larger format configurations. Two-side butttable 2052×2052 arrays can be arranged in a 4104×4104 format (with 64 outputs), as illustrated in Fig. 26. The three-side butttable arrays can be arranged in $2 \times n$ array configurations to build up large rectangular formats [34,47].

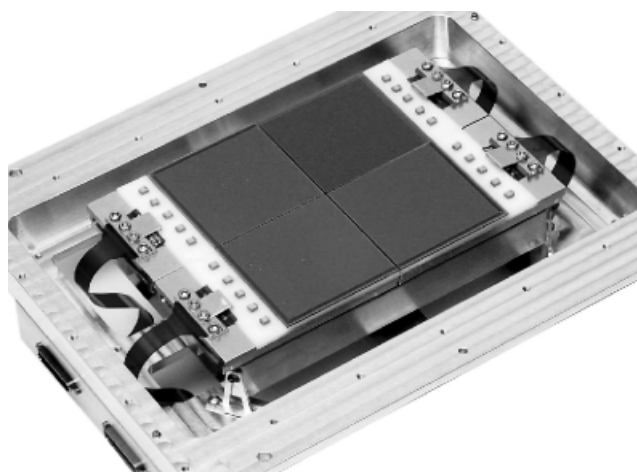


Fig. 26. Four two-side butttable 2052×2052 InSb arrays in a mosaic configuration 4104×4104 arrays pixels (after Ref. 47).

5.4.5. HgCdTe arrays

HgCdTe photodiodes are available to cover the spectral range from 1 to $20\text{ }\mu\text{m}$. Spectral cutoff can be tailored by adjusting the HgCdTe alloy composition. Most applications are concentrated in the SWIR ($1\text{--}3\text{ }\mu\text{m}$), MWIR ($3\text{--}5\text{ }\mu\text{m}$), and LWIR ($8\text{--}12\text{ }\mu\text{m}$). Also development work on improving performance of very LWIR (VLWIR) photodiodes in the $13\text{--}18\text{ }\mu\text{m}$ region for important earth-monitoring applications are undertaken.

Epitaxy is the preferable technique to obtain device-quality HgCdTe epilayers for IR devices. The epitaxial techniques offer the possibility to grow large area epilayers and sophisticated layered structures with abrupt and complex composition and doping profiles.

Among the various epitaxial techniques, the LPE is the most matured method. The recent efforts are mostly on low

growth temperature techniques; MBE and MOCVD. MBE offers unique capabilities in material and device engineering including the lowest growth temperature, superlattice growth and potential for the most sophisticated composition and doping profiles. The growth temperature is less than 200°C for MBE but around 350°C for MOCVD, making it more difficult to control the p-type doping in the MOCVD due to the formation of Hg vacancies.

Different HgCdTe photodiode architectures have been fabricated that are compatible with backside illuminated hybrid FPA technology [46,48,49]. The realization of HgCdTe photodiodes has usually based on the most common ion implanted n⁺-p (n-on-p) and heterojunction P⁺-n (p-on-n) structure (capital letter denotes wider gap). In these photodiodes the base p-type layers (or n-type layers) are sandwiched between CdZnTe substrate and high-doped (in n⁺-p structures) or wider-gap (in P⁺-n structure) regions. Due to backside illumination (through CdZnTe substrate) and internal electric fields (which are “blocking” for minority carriers), influence of surface recombination on the photodiodes performance is eliminated. Both optical and thermal generations are suppressed in the n⁺-region due to the Burstein-Moss effect and in the P⁺-region due to wide gap. The influence of surface recombination is also prevented by the use of suitable passivation. Recently, most laboratories have been using CdTe or CdZnTe (deposited by MBE, MOCVD, sputtering and e-beam evaporation) for photodiode passivation.

The structure of a mesa-etched p-on-n photodiode is illustrated in Fig. 27(a). In this so-called double-layer

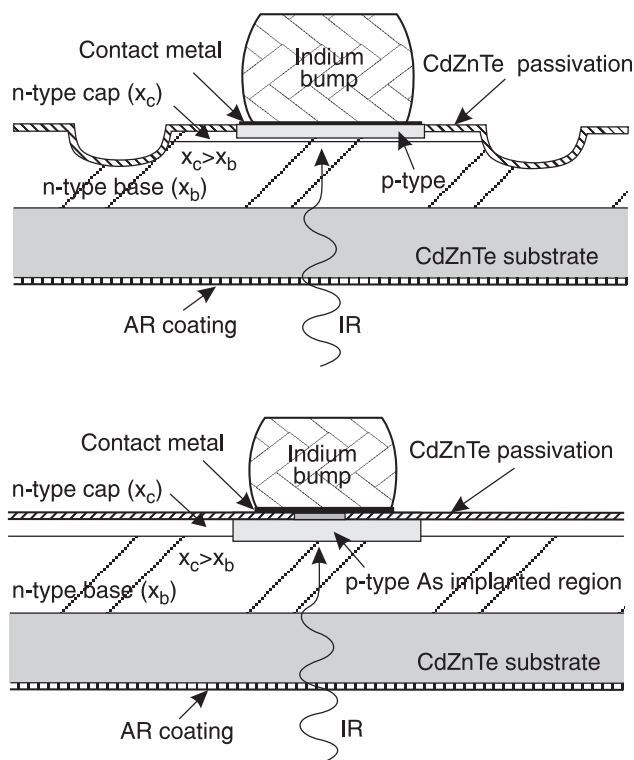


Fig. 27. Cross sections of p-on-n DLHJ HgCdTe photodiodes: (a) mesa structure, (b) planar structure.

heterojunction (DLHJ) structure, about 10-μm thick absorber layer is doped with indium at $1 \times 10^{15} \text{ cm}^{-3}$ or less. Contacts are made to the p⁺-layer in each pixel and to n-type layer at the edge of the array (not shown).

The formation of planar p-on-n photodiodes [see Fig. 27(b)] is achieved by selective area arsenic ion-implantation through the cap layer into the narrow gap base layer. The implantation step is achieved by a two-step thermal anneal under Hg overpressure: one at high temperature activates the dopant by substituting As atoms on the Te sublattice, while the second at lower temperature – annihilates the Hg vacancies formed in the HgCdTe lattice during growth and high temperature annealing step.

The other type of structure applied in second and third generation IR systems is shown in Fig. 28. It is vertical integrated photodiode (VIPTM) elaborated in DRS Infrared Technologies. This structure is similar to British loophole photodiode [see Fig. 10(b)]. This n⁺-n⁻-p architecture is formed around the via, both by etching process itself and subsequent ion implant step after the layer has been glued to the readout and thinned. Low background indium n⁻-doping levels of 1.5 to $5 \times 10^{14} \text{ cm}^{-3}$ are routinely used. The p⁺-p non-injection contacts are formed in each cell of the FPA and are joined electrically by a top surface metal grid as shown in Fig. 28. To connect the n-type regions with the readout inputs, the contacts are deposited through the via holes. In contrast to the mesa and planar structures, this device is front-side illuminated.

Up to the present, photovoltaic HgCdTe FPAs have been mainly based on p-type material. Linear (240, 288, 480, and 960 elements), 2D scanning arrays with time delay and integration (with common formats of 256×4, 288×4, 480×6), and 2D staring formats from 64×64 up to 2048×2048 have been made with a wide range of spectral response [4]. Efforts are also underway to develop avalanche photodiode capabilities in the 1.6-μm and at longer wavelength region. Pixel sizes ranging from 18-μm square to over 1 mm have been demonstrated.

The best results have been obtained using hybrid architecture. However, the very large hybrid structures suffer from mechanically fatigue problems that result from different thermal expansion between the detector and readout structures. Therefore considerable effort is being extended to develop techniques for growing HgCdTe on silicon substrates.

Rockwell has developed the world's largest HgCdTe short wavelength IR (SWIR) FPA for astronomy and low background applications (see Fig. 29) [51,52]. The format of the device is a hybrid 2048×2048 with a unit cell size of 18-μm×18-μm and with active size of 37 mm. Sets of four arrays will be “tiled” into 2×2 mosaic configurations giving 4096×4096 pixels [53]. One of the 4096×4096 mosaic will be installed in camera instrument on Mauna Kea, Hawaii, and the other mosaic will be installed in IR imager on Gemini South in Chile. Development of large format, high sensitivity, mosaic IR sensors for ground-based astronomy is the goal of many observatories around the world (large

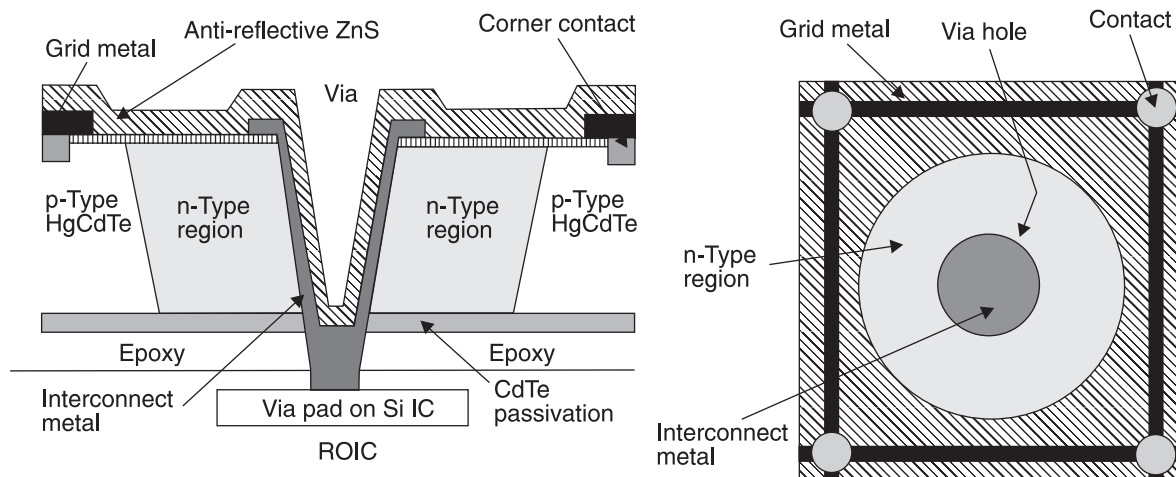


Fig. 28. DRS' high-density vertically integrated photodiode (HDVIP™) n^+-n^-p HgCdTe photodiode (after Ref. 50).

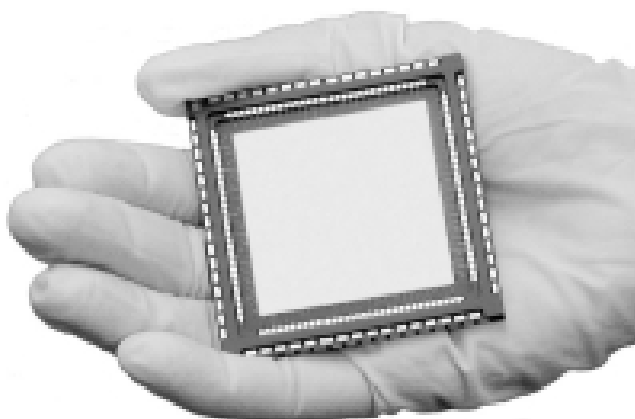


Fig. 29. A 2048×2048 SWIR (1–3 μm) HgCdTe Hawaii array with 18- μm pixels (after Ref. 4).

arrays dramatically multiply the data output of a telescope system). This is somewhat surprising given the comparative budgets of the defence market and the astronomical community.

5.4.6. QWIP arrays

An alternative hybrid detector for the long wavelength IR region (8–14- μm) is the quantum well infrared photoconductors (QWIPs). These high impedance detectors are built from alternating thin layers (superlattices) of GaAs and AlGaAs. Despite large research and development efforts, large photovoltaic HgCdTe FPAs remain expensive, primarily because of the low yield of operable arrays. The low yield is due to sensitivity of LWIR HgCdTe devices to defects and surface leakage, which is a consequence of basic material properties. A serious problem in the case of LWIR HgCdTe detectors is their nonuniformity. With respect to HgCdTe detectors, GaAs/AlGaAs quantum well devices have a number of potential advantages, including the use of standard manufacturing techniques based on mature GaAs growth and processing technologies, highly uni-

form and well-controlled MBE growth on greater than 6 in. GaAs wafers, high yield and thus low cost, more thermal stability, and extrinsic radiation hardness.

A distinct feature of n-type QWIPs is that the optical absorption strength is proportional to the electric-field polarization component of an incident photon in a direction normal to the plane of the quantum wells. For imaging, it is necessary to couple light uniformly to 2D arrays of these detectors, so a diffraction grating is incorporated on one side of the detectors to redirect a normally incident photon into propagation angles more favourable for absorption (see Fig. 30).

QWIP detectors have relatively low quantum efficiencies, typically less than 10%. The spectral response band is also narrow for this detector, with a full-width, half-maximum of about 15%. All the QWIP data with cutoff wavelength about 9 μm is clustered between 10^{10} and 10^{11} $\text{cm}^2\text{Hz}^{1/2}/\text{W}$ at about 77 K operating temperature. Investigations of the fundamental physical limitations of HgCdTe photodiodes indicate better performance of this

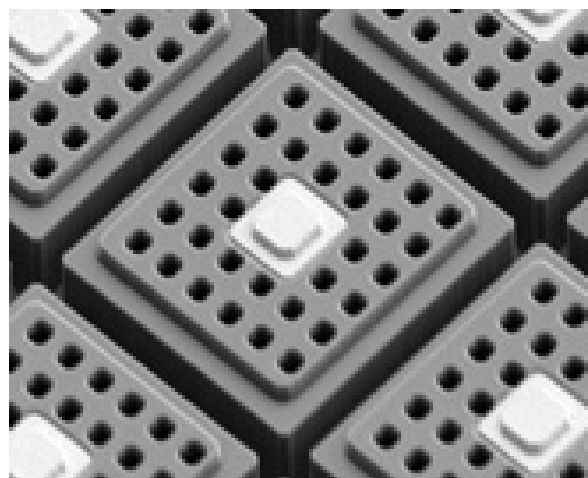


Fig. 30. SEM view of QWIP detector. A two-dimensional grating structure provides diffraction to couple light uniformly across the array (after Ref. 54).

type of detector in comparison with QWIPs operated in the range 40–77 K. However, it has been shown, that a low photoconductive gain actually increases the signal-to-noise ratio [55] and a QWIP FPA can have a better temperature resolution than an HgCdTe FPA with similar storage capacity. This deduction was experimentally confirmed by Schneider *et al.* [56]. Several camera systems with $NEDT < 10$ mK and $NEDT < 20$ mK for FPAs with 256×256 and 640×512 pixels have been demonstrated [57,58]. Recently, the first results of megapixel QWIP array have been presented [59]. The GaAs/AlGaAs QWIPs are also well situated to multi-colour IR sensors. This topic is considered in section 5.6.

5.4.7. Thermal detector arrays

The use of thermal detectors for IR imaging has been the subject of research and development for many decades. Thermal detectors are not useful for high-speed scanning thermal imagers. Only pyroelectric vidicons have found more widespread use. These devices achieved their fundamental limits of performance by about 1970. However, the speed of thermal detectors is quite adequate for non-scanned imagers with 2D detectors. With large arrays of thermal detectors the best values of $NEDT$ below 0.1 K could be reached because effective noise bandwidths less than 100 Hz can be achieved. This compares with a bandwidth of several hundred kilohertz for conventional cooled thermal imagers with a small photon detector array and scanner. Realization of this fact caused a new revolution in thermal imaging, which is underway now [60,61]. This is due to the development of 2D electronically scanned arrays, in which moderate sensitivity can be compensated by a large number of elements. Large scale integration combined with micromachining has been used for manufacturing of large 2D arrays of uncooled IR sensors. This enables fabrication of low cost and high-quality thermal imagers. Although developed for military applications, low-cost IR imagers are used in nonmilitary applications such as: drivers aid, aircraft aid, industrial process monitoring, community services, firefighting, portable mine detection, night vision, border surveillance, law enforcement, search and rescue, etc.

Figure 31 shows a $50\text{-}\mu\text{m}$ pixel in the most common uncooled microbolometer device structure. The microbolometer consists of a $0.5\text{ }\mu\text{m}$ thick bridge of Si_3N_4 suspended about $2\text{ }\mu\text{m}$ above the underlying silicon substrate. The use of a vacuum gap of approximately $2.5\text{ }\mu\text{m}$, together with a quarter wave resonant cavity between the bolometer and the underlying substrate, can produce a reflector for wavelengths near $10\text{ }\mu\text{m}$. The bridge is supported by two narrow legs of Si_3N_4 , which provide the thermal isolation between the microbolometer and the heat-sink readout substrate. Long, thin legs are anchored to the readout surface. The most popular thermistor materials used in fabrication of the monolithic bolometer structures are vanadium dioxide (VO_x)

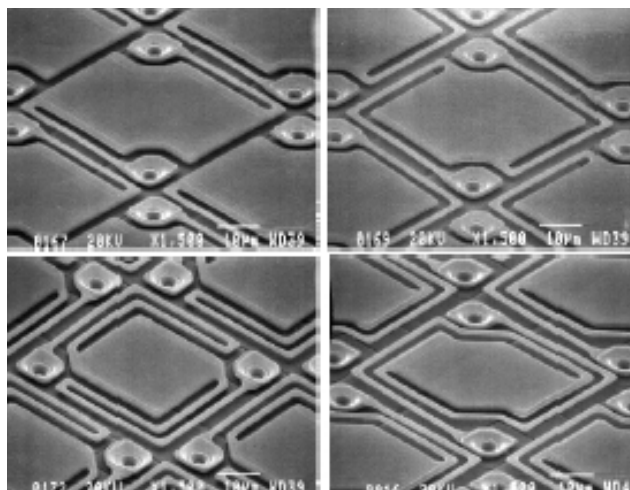


Fig. 31. Monolithic uncooled microbolometers with $50\text{-}\mu\text{m}$ pixels. Clockwise from upper left: isolation arm on the side, two sides, and twice on two sides. Improving of thermal isolation, which is achieved with long leg lengths, sacrifices the fill factor (after Ref. 4).

or amorphous silicon suspended above the surface in a large resistive pad. Both materials are characterized by high thermal coefficient of resistance, typically about $2\%/K$.

The detection range of many uncooled IR imaging systems is limited by pixel resolution rather than sensitivity. However, the $NEDT$ is inversely proportional to the pixel area. So, the development of highly sensitive $25\text{-}\mu\text{m}$ microbolometer pixels presents significant challenges in both fabrication process improvements and in pixel design. The $f/1$ $NEDT$ performance of $25\text{-}\mu\text{m}$ pitch microbolometer FPAs is projected to be below 20 mK [62]. Figure 32 illustrates an infrared image from large 480×640 array format with $NEDT$ below 0.1 K.

Also pyroelectric detectors are used for thermal imaging, but in hybrid configuration. The imaging systems based on pyroelectric arrays, usually need to be operated with optical modulators, which chop or defocus the incom-



Fig. 32. Infrared image taken by a 480×640 pixel microbolometer. These devices can detect temperature variations smaller than 0.1 K (after Ref. 4).

ing radiation. This may be an important limitation for many applications in which chopperless operation is highly desirable (e.g., guided munitions).

Hybrid pyroelectric/ferroelectric bolometer detector [barium strontium titanate (BST) ceramic] was the first to enter production, and is the most widely used type of thermal detector (in the U.S., the Cadillac Division of General Motors has pioneered this application, selling thermal imagers to the customer for just under \$2000) [63]. Although many applications for this hybrid array technology have been identified, and imagers employing these arrays are in mass production, no hybrid technology advances are foreseen. The reason is that the thermal conductance of the bump bonds is so high that the array *NETD* (*f*/1 optics) is limited to about 50 mK. Pyroelectric array technology therefore is moving toward monolithic silicon microstructure technology. The monolithic process should have fewer steps and shorter cycle time. Most ferroelectrics tend to lose their interesting properties as the thickness is reduced. However, some ferroelectric materials seem to maintain their properties better than others. This seems particularly true for lead titanate and related materials, whereas BST, the material does not hold its properties well in thin-film form.

5.5. Far infrared detector arrays

Extrinsic silicon detectors can form high impedance photoconductors in a hybrid configuration and can be operated out to about 30 μm . Shallow, hydrogen-like impurities, such as phosphorus, antimony, or arsenic, provide electrons which can be ionised with photon energies in the range of 30–50 meV, depending upon the dopant and concentration used. These devices must be cooled to below 20 K to prevent significant thermal ionization.

The limit to the useful doping which is possible in conventional extrinsic detectors is set by the onset of impurity banding. This occurs when the doping level is sufficiently high that the wavefunctions of neighbouring impurities overlap and their energy level is broadened to a band which can support hopping conduction. When this occurs it limits the detector resistance and photoconductive gain, and also increases the dark current and noise. To overcome the impurity banding effect and in addition, to improve radiation hardness and reduce the optical cross-talk between adjacent elements of an array, the blocked impurity band (BIB) device was proposed.

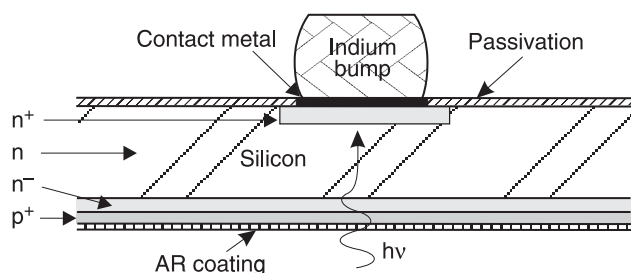


Fig. 33. Blocked impurity band hybrid detector.

A BIB detector structure is displayed in Fig. 33. This structure usually have a thin lightly-doped n^- -region (usually grown epitaxially) between the absorbing n -type region and the common backside implant (p^+ -region) in order to block hopping-conduction currents from reaching the p^+ -contact, which are substantial at the doping levels used in the active detection region. Doping of active layer with a thickness value in the 10- μm range is high enough for the onset of an impurity band in order to display high quantum efficiency for impurity ionization. This also prevents the build of large space-charge regions in n -type active regions, which can otherwise result in a dielectric relaxation response that depends on the illumination history.

BIB devices, in large staring array formats are now becoming commercially available. Impressive progress has been achieved especially in Si:As BIB array technology with formats as large as 1024 \times 1024 (pixel size 27- μm) operated in spectral band up to 30 μm at 10 K [47]. Their main application today is for ground and space-based far-infrared astronomy.

Due to lack of atmospheric transparency in the far-infrared region (above 30 μm), applications are limited to the laboratory, high altitude and space. Germanium extrinsic detectors have largely been supplanted by silicon detectors for both high and low background applications where comparable spectral response can be obtained, but germanium devices are still of interest for very long wavelengths. Very shallow donors, such as Sb, and acceptors, such as B, In or Ga, provide cut-off wavelengths in the region of 100 μm .

Ge:Ga photoconductors are the best low background photon detectors for the wavelength range from 40 to 120 μm . Application of uniaxial stress along the [100] axis of Ge:Ga crystals reduces the Ga acceptor binding energy, extending the cutoff wavelength to \approx 240 μm . At the same time, the operating temperature must be reduced to less than 2 K. In making practical use of this effect, it is essen-

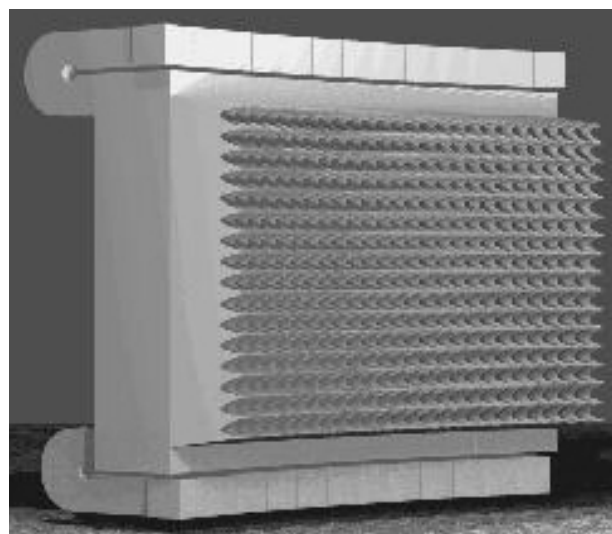


Fig. 34. Stressed Ge:Ga detector array (FIFI-LS) in a 16 \times 25 pixel format (after Ref. 64).

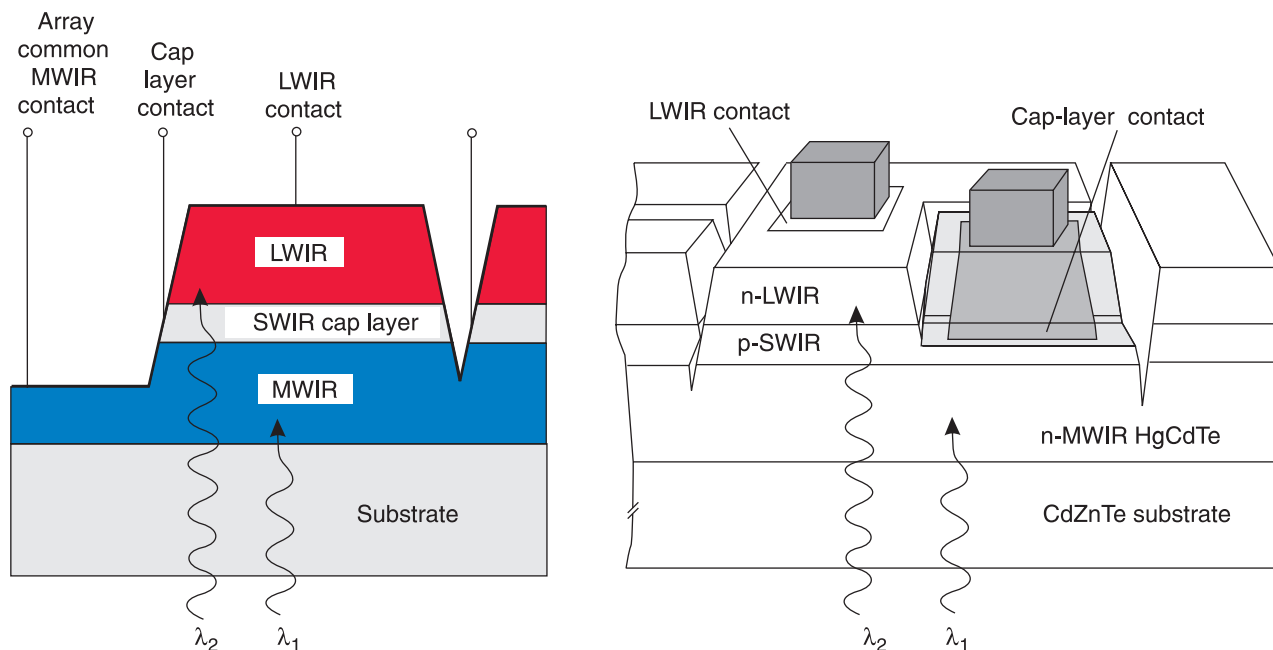


Fig. 35. Cross section of integrated two-colour HgCdTe detectors in an n-p-n layer structure for simultaneous operating mode. A thin p-type barrier separates the two absorbing bands.

tial to apply and maintain very uniform and controlled pressure to the detector so that the entire detector volume is placed under stress without exceeding its breaking strength at any point. A number of mechanical stress modules have been developed. The stressed Ge:Ga photoconductor systems have found a wide range of astronomical and astrophysical applications. For example, Fig. 34 shows a 16×25 pixel stressed germanium array being developed for the Herschel Space Observatory and SOFIA to provide observations in the far-infrared out to $200 \mu\text{m}$. Each detector pixel is stressed in its own subassembly, and a signal wire is routed to preamplifiers housed nearby what obviously limits this type of array to much smaller formats than are available without this constraints.

5.6. Third generation infrared detectors

In the infrared spectral region, third generation systems are now being developed. In this class of detector, two main competitors, HgCdTe photodiodes and QWIPs are considered [65]. Third generation IR systems considered to be those that provide enhanced capabilities like larger number of pixels, higher frame rates, better thermal resolution as well as multicolour functionality and other on-chip functions. Multicolour capabilities are highly desirable for advance IR systems. Systems that gather data in separate IR spectral bands can discriminate both absolute temperature and unique signatures of objects in the scene. By providing this new dimension of contrast, multiband detection also offers advanced colour processing algorithms to further improve sensitivity compared to that of single-colour devices.

Two-colour array capability is based upon stacking materials with different spectral responses on top of each

other. The shorter wavelength flux is absorbed in the first layer which then transmits the longer wavelength flux through the second layer. One such structure – a HgCdTe two-colour device, with two indium bumps per pixel is illustrated in Fig. 35.

Two-colour QWIP detector structures have also been built [66]. For example, Fig. 36 shows the excellent imagery in each colour. Note the appearance of the front-held optical filter and the vertically-held hot soldering iron in the two bands. At present, however, imaging systems using two-colour arrays are in limited use. Some considerations have suggested that three-colour FPAs would be more generally useful.

Recently, a four-colour QWIP FPA has been demonstrated by stacking different multi-quantum well structures, which are sensitive in $4\text{--}6$, $8.5\text{--}10$, $10\text{--}12$, and $13\text{--}15 \mu\text{m}$ bands [58]. The 640×512 format FPA consists of four 640×128 pixel areas which are capable of acquiring images in these bands. Four separate detector bands were defined



Fig. 36. Simultaneous images from 256×256 MWIR/LWIR QWIP FPAs. Note appearance of the front-held filter and the hot soldering iron in the two bands (after Ref. 66).

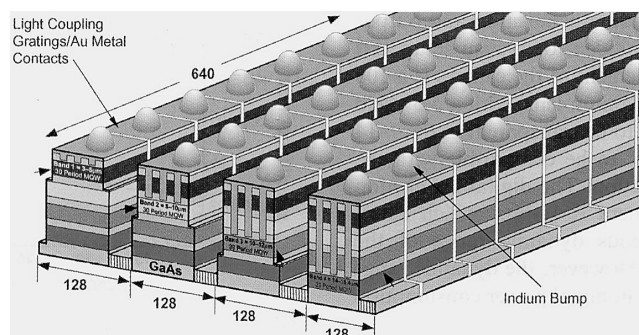


Fig. 37. Layer diagram of the four-band QWIP device structure and the deep groove 2-D-periodic grating structure. Each pixel represents a 640×128 pixel area of the four-band FPA (after Ref. 67).

by a deep trench etch process and the unwanted spectral bands were eliminated by a detector short-circuiting process. The unwanted top detectors were electrically shorted by gold-coated reflective 2D etched gratings as shown in Fig. 37. Figure 38 shows one frame of a video image taken with the four-band 640×512 pixel QWIP FPA. It is noticeable that the object in the $13\text{--}15\text{ }\mu\text{m}$ band is not very clear due to the reduced optical transmission of the germanium lens beyond $14\text{ }\mu\text{m}$.

It should be mentioned that hyperspectral arrays are distinguished from multispectral ones in typically having a hundred or more bands. HgCdTe, and other detector materials such as silicon and InSb, have been used in hyperspectral assemblies in the form of 2D arrays with a closely-packed layout of rows and columns. A prism, grating, or a "wedged" filter is used to illuminate each row with a different wavelength. Figure 39 shows an example of a hyperspectral array.

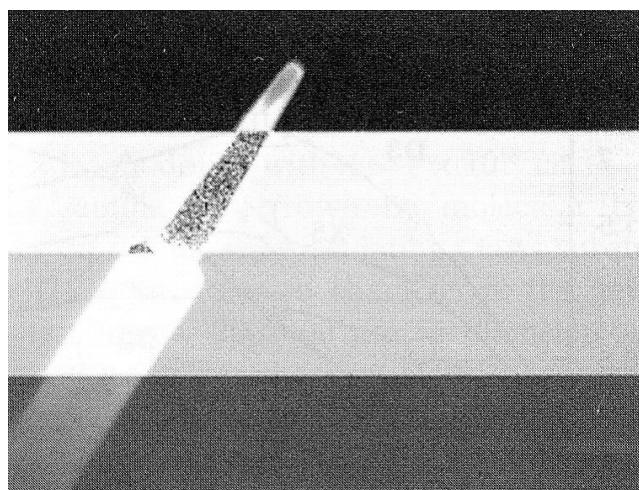


Fig. 38. One frame of video image taken with the $4\text{--}15\text{ }\mu\text{m}$ cutoff four-band 640×512 pixel QWIP camera. The image is barely visible in the $13\text{--}15\text{ }\mu\text{m}$ spectral band due to the poor optical transmission of the anti-reflection layer coated germanium lens (after Ref. 67).

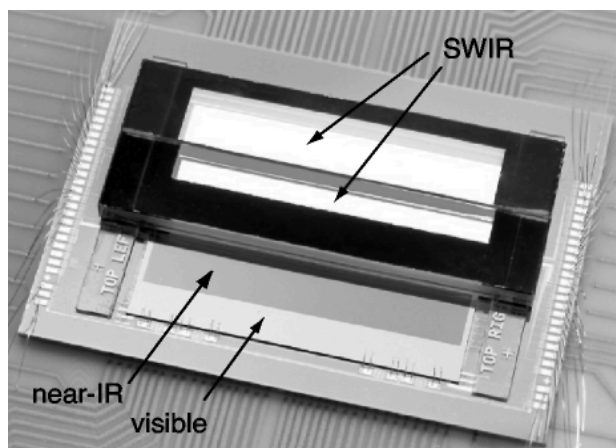


Fig. 39. Hyperspectral array with 300 bands made from silicon and HgCdTe together with four wedge filters. The array has 100 spectral bands in the range from 0.4 to $1.0\text{ }\mu\text{m}$, and 200 from 1.0 to $2.5\text{ }\mu\text{m}$ (after Ref. 4).

6. Conclusions

This paper reviews optical detector focal plane array technology with emphasis on the past 25 years. Discussion is focused mainly on current and the most rapidly developing detectors: CdZnTe detectors, AlGaIn photodiodes, visible CCD and CMOS imaging systems, HgCdTe heterostructure photodiodes, quantum well AlGaAs/GaAs photoconductors, and thermal detectors. It is shown that in the spectral range from X ray to far infrared the rate at which images can be acquired has increased by more than a factor of a million in many cases. Even in visible region, the detector arrays are gradually replacing film as the capabilities and popularity of digital camera grow.

The second aspect of presentation devotes trends in focal plane array technology. Examples of arrays and imagers are chosen to illustrate the current state and art. All considerations are carried out in historical aspects.

This paper offers a rather wide coverage of optical detector technology. However, for a full understanding of the technical content, the paper requires as a prerequisite the basic courses in material science and fundamentals of semiconductor physics.

References

1. P.W. Kruse, L.D. McGlauchlin, and R.B. McQuistan, *Elements of Infrared Technology*, Wiley, New York, 1962.
2. P.W. Kruse, "The photon detection process", in *Optical and Infrared Detectors*, pp. 5–69, edited by R.J. Keyes, Springer-Verlag, Berlin, 1977.
3. D.H. Seib and L.W. Aukerman, "Photodetectors for the 0.1 to $1.0\text{ }\mu\text{m}$ spectral region", in *Advances in Electronics and Electron Physics*, Vol. 34, pp. 95–221, edited by L. Morton, Academic Press, New York, 1973.
4. P. Norton, "Detector focal plane array technology", in *Encyclopedia of Optical Engineering*, edited by R. Driggers, pp. 320–348, Marcel Dekker Inc., New York, 2003.

5. L.J. Kozlowski, J. Montroy, K. Vural, and W.E. Kleinmans, "Ultra-low noise infrared focal plane array status", *Proc. SPIE* **3436**, 162–171 (1988).
6. L.J. Kozlowski, K. Vural, J. Luo, A. Tomasini, T. Liu, and W.E. Kleinmans, "Low-noise infrared and visible focal plane arrays", *Opto-Electron. Rev.* **7**, 259–269 (1999).
7. E.R. Fossum, "Active pixel sensors: Are CCD's dinosaurs?", *Proc. SPIE* **1900**, 2–14 (1993).
8. E.R. Fossum and B. Pain, "Infrared readout electronics for space science sensors: State of the art and future directions", *Proc SPIE* **2020**, 262–285 (1993).
9. P.R. Norton, "Photodetectors", in *Handbook of Optics*, Vol. 1, 15.3–15.100, edited by M. Bass, E.W. Van Stryland, D.R. Williams, and W.L. Wolfe, McGraw-Hill, Inc., New York, 1995.
10. S. Donati, *Photodetectors. Devices, Circuits, and Applications*, Prentice Hall Inc., 1999.
11. A. Rogalski, *Infrared Detectors*, Gordon and Breach Science Publishers: Amsterdam, 2000.
12. A. Rogalski, "Photon detectors", in *Encyclopedia of Optical Engineering*, pp. 1985–2035, edited by R. Driggers, Marcel Dekker, Inc., New York, 2003.
13. J.M. Backer and R.A. Ballinga, "Photovoltaic CdHgTe-silicon hybrid focal planes", *Proc. SPIE* **510**, 121–129 (1984).
14. A. Rogalski and Z. Bielecki, "Detection of optical radiation", *Bull. Pol. Ac.: Tech.* **52**, ? (2004).
15. http://chandra.harvard.edu/about/science_instruments.html
16. <http://chandra.harvard.edu/about/focalplane.html>
17. <http://www.varian.com/xry/prd004.html>
18. T. Whitaker, "CdZnTe radiation detectors", *Compound Semiconductors* **5**, 39–40 (1999).
19. <http://www.evproducts.com>
20. H.B. Barber, H.H. Barrett, F.L. Augustine, W.J. Hamilton, B.A. Apotovsky, E.L. Dereniak, F.P. Doty, J.D. Eskin, J.P. Garcia, D.G. Marks, K.J. Matherson, J.M. Woelfenden, and E.T. Young, "Development of a 64×64 CdZnTe array and associated readout integrated circuit for use in nuclear medicine", *J. Electron. Mater.* **26**, 765–772 (1997).
21. M. Razeghi and A. Rogalski, "Semiconductor ultraviolet detectors", *J. Appl. Phys.* **79**, 7433–7473 (1996).
22. D. Walker and M. Razeghi, "The development of nitride-based UV photodetectors", *Opto-Electron. Rev.* **8**, 25–42 (2000).
23. F. Monroy, F. Omnes, and F. Calle, "Wide-bandgap semiconductor ultraviolet photodetectors", *Semicon. Sci. Technol.* **18**, R33–R51 (2003).
24. Y.S. Park, "Wide bandgap III-Nitride semiconductors: Opportunities for future optoelectronics", *Opto-Electron. Rev.* **9**, 117–124 (2001).
25. J.P. Long, S. Varadaraajan, J. Matthews, and J.F. Schetzina, "UV detectors and focal plane array imagers based on AlGaIn p-i-n photodiodes", *Opto-Electron. Rev.* **10**, 251–260 (2002).
26. UDT Sensors, Inc., Catalogue.
27. J.R. Janesick, *Scientific Charge-Coupled Devices*, SPIE Press, Bellingham, 2001.
28. J.R. Janesick, "Charge-coupled CMOS and hybrid detector arrays", *Proc. SPIE* **5167**, 1–18 (2003).
29. "X-3: New single-chip colour CCD technology", *New Technology*, 20–24, March/April 2002.
30. <http://www.kodak.com>
31. <http://www.foveon.com>
32. <http://www.alt-vision.com>
33. <http://www.dalsa.com>
34. A.W. Hoffman, P.J. Love, and J.P. Rosbeck, "Mega-pixel detector arrays: visible to 28 μm ", *Proc. SPIE* **5167**, 194–212 (2003).
35. J. John, L. Zimmermann, S. Nemeth, T. Colin, P. Merken, S. Borghs, and C. Van Hoof, "Extended InGaAs on GaAs detectors for SWIR linear sensors", *Proc. SPIE* **4369**, 692–697 (2001).
36. M.H. Ettenberg, M.J. Lange, M.T. O'Grady, J.S. Vermaak, M.J. Cohen, and G.H. Olsen, "A room temperature 640×512 pixel near-infrared InGaAs focal plane array", *Proc. SPIE* **4028**, 201–207 (2000).
37. F.D. Shepherd and A.C. Yang, "Silicon Schottky retinas for infrared imaging", *Tech. Digest of IEDM*, 310–313 (1973).
38. W.F. Kosonocky, "Review of infrared image sensors with Schottky-barrier detectors", *Optoelectronics – Devices and Technologies* **6**, 173–203 (1991).
39. M. Kimata, N. Yutani, N. Tsubouchi and T. Seto, "High performance 1040×1040 element PtSi Schottky-barrier image sensor", *Proc. SPIE* **1762**, 350–360 (1992).
40. M. Kimata and N. Tsubouchi, "Schottky barrier photoemissive detectors", in *Infrared Photon Detectors*, pp. 299–349, edited by A. Rogalski, SPIE Optical Engineering Press, Bellingham, 1995.
41. M. Kimata, M. Ueno, H. Yagi, T. Shiraishi, M. Kawai, K. Endo, Y. Kosasayama, T. Sone, T. Ozeki, and N. Tsubouchi, "PtSi Schottky-barrier infrared focal plane arrays", *Opto-Electron. Rev.* **6**, 1–10 (1998).
42. R.J. Cashman, "Film-type infrared photoconductors", *Proc. IRE* **47**, 1471–1475 (1959).
43. H. Zogg, "Lead chalcogenide on silicon infrared sensor arrays", *Opto-Electron. Rev.* **6**, 37–46 (1998).
44. <http://www.littoneos.com>
45. K. Alchalabi, D. Zimin, H. Zogg, and W. Buttler, "Monolithic heteroepitaxial PbTe-on-Si infrared focal plane array with 96×128 pixels", *IEEE Electron Dev. Lett.* **22**, 110–112 (2001).
46. A. Rogalski, K. Adamiec, and J. Rutkowski, *Narrow-Gap Semiconductor Photodiodes*, SPIE Press: Bellingham, 2000.
47. P.J. Love, K.J. Ando, R.E. Bornfreund, E. Corrales, R.E. Mills, J.R. Cripe, N.A. Lum, J.P. Rosbeck, and M.S. Smith, "Large-format infrared arrays for future space and ground-based astronomy applications", *Proc. SPIE* **4486**, 373–384 (2002).
48. M.B. Reine, "Photovoltaic detectors in MCT", in *Infrared Detectors and Emitters: Materials and Devices*, pp. 279–312, edited by P. Capper and C.T. Elliott, Kluwer Academic Publishers, Boston, 2000.
49. P. Norton, "HgCdTe infrared detectors," *Opto-Electron. Rev.* **10**, 159–174 (2002).
50. M.A. Kinch, "HDVIP™ FPA technology at DRS", *Proc. SPIE* **4369**, 566–578 (2001).
51. K. Vural, L.J. Kozlowski, D.E. Cooper, C.A. Chen, G. Bostrup, C. Cabelli, J.M. Arias, J. Bajaj, K.W. Hodapp, D.N.B. Hall, W.E. Kleinmans, G.G. Price, and J.A. Pinter, "2048×2048 HgCdTe focal plane arrays for astronomy applications", *Proc. SPIE* **3698**, 24–35 (1999).
52. <http://www.rsc.rockwell.com/imaging/>

53. <http://compoundsemiconductor.net/articles/news/6/8/5/1>
54. <http://www.iaf.fhg.de/buisqwfp/>
55. A. Rogalski, "Quantum well photoconductors in infrared detector technology", *J. Appl. Phys.* **93**, 4355–4391 (2003).
56. H. Schneider, M. Walther, J. Fleissner, R. Rehm, E. Diwo, K. Schwarz, P. Koidl, G. Weimann, J. Ziegler, R. Breiter, and W. Cabanski, "Low-noise QWIPs for FPA sensors with high thermal resolution", *Proc. SPIE* **4130**, 353–362 (2000).
57. H. Schneider, P. Koidl, M. Walther, J. Fleissner, R. Rehm, E. Diwo, K. Schwarz, and G. Weimann, "Ten years of QWIP development at Fraunhofer", *Infrared Phys. Technol.* **42**, 283–289 (2001).
58. S.D. Gunapala, S.V. Bandara, J.K. Liu, B. Rafol, and J.M. Mumolo, "640×512 pixel long-wavelength infrared narrowband, multiband, and broadband QWIP focal plane arrays", *IEEE Trans. Electron Devices* **50**, 2353–2360 (2004).
59. M. Jhabvala, K. Choi, A. Goldberg, A. La, and S. Gunapala, "Development of a 1k×1k GaAs QWIP far IR imaging array", *Proc. SPIE* **5167**, 175–185 (2004).
60. *Semiconductors and Semimetals*, Vol. 47, edited by P.W. Kruse and D.D. Skatrud, Academic Press, San Diego (1997).
61. P.W. Kruse, "Uncooled IR focal plane arrays", *Opto-Electron. Rev.* **7**, 253–258 (1999).
62. D. Murphy, M. Ray, R. Wyles, J. Asbrock, N. Lum, A. Kennedy, J. Wyles, C. Hewitt, G. Graham, W. Radford, J. Anderson, D. Bradley, R. Chin, and T. Kostrzewa, "High sensitivity (25 μm pitch) microbolometer FPAs and application development", *Proc. SPIE* **4369**, 222–234 (2001).
63. P.W. Kruse, *Uncooled Thermal Imaging. Arrays, Systems, and Applications*, SPIE Press, Bellingham, 2001.
64. <http://fifi-ls.mpg-garching.mpg.de/detector.html>
65. A. Rogalski, "Third-generation infrared photon detectors", *Opt. Eng.* **42**, 3498–3516 (2003).
66. T. Whitaker, "Sanders' QWIPs detect two colour at once", *Compound Semiconductors* **5**, 48–51, 1999.
67. S.D. Gunapala, S.V. Bandara, J.K. Liu, B. Rafol, J.M. Mumolo, C.A. Shott, R. Jones, J. Woolaway, J.M. Fastenau, A.K. Liu, M. Jhabvala, and K.K. Choi, "640×512 pixel narrow-band, four-band, and broad-band quantum well infrared photodetector focal plane arrays," *Infrared Phys. Technol.* **44**, 411–425 (2003).

EUROCONFERENCE Photovoltaic Devices



EUROPV 2004



Kranjska Gora, Slovenia, October 15–20, 2004

SCOPE OF THE CONFERENCE

The aim of the conference is to apply the results from the first conference Photovoltaics and Environment (Granada, 2003) and focus on the large-scale production and application of PV in the future. Ecological and economical aspects of mass production of the different cell types in the GW-scale will be examined and speakers with a broad experience in today's PV-production will give their views on existing production methods, possible future improvements and up-scaling. The mass application of PV as a major source of electricity will be scrutinised with respect to the impact on the grids, usage of existing buildings and open space. The conference will provide an intense forum to researchers from industry and academic institutions to exchange their views on new developments and strategies as well as to form new collaborations. The set up of the programme is multidisciplinary in order to promote the cross-fertilisation of different disciplines, technologies and developments. Leading scientists and representatives from companies will refer about the latest research results and developments. In addition there will be poster sessions, informal working group sessions and round table discussions. To assure an efficient exchange and transfer of the knowledge of the photovoltaics and environment the number of the participants will be limited to about 100. Grants will be available for younger scientists and INCO scientists waiving the registration fee.

LANGUAGE

English is the official language.

CONFERENCE SITE

Hotel Larix, (<http://www.htp-gorenjka.si/>)
Borovška cesta 99, Si-4280 Kranjska Gora, Slovenia

REGISTRATION FEE

Registration fees include Accommodation & Full Board, Excursion and bus transfer from/to airport Ljubljana

INVITED SPEAKERS

Dr. Jesus Alonso (Isofoton, Spain)
Dr. Derk Blätzner (ETH Zürich, Switzerland)
Artur Buechel (Unaxis, Lichtenstein)
Dr. Net Daukes (Imperial College London, UK)
Dr. Alessandro Fraleoni-Morgera (University of Bologna, Italy)
Dr. Jonathan Halls (CDT, Cambridge (UK))
Dr. Arnulf Jäger Waldau (European Commission JRC Ispra, Italy)
Dr. Gert Jan Jorgenden (Akzo Nobel, The Netherlands)
Prof. Daniel Lincot (Laboratoire d'Electrochimie ENSCP, France)
Dr. Tobias Meyer (Solaronix SA, Switzerland)
Pietro Menna (European Commission DG TREN, Belgium)
Dr. Ersin Ozsan (Teksolar, UK)
Dr. Jef Poortmans (IMEC, Belgium)
Dr. Volker Probst (Shell Solar, Germany)
Dr. Bernd Rech (Forschungszentrum Jülich, Germany)
Prof. Wim Sinke (ECN, The Netherlands)
Dr. Jozef Szlufcik (Photovoltech, Belgium)
Dr. Karsten Wambach (Deutsche Solar, Germany)
Prof. Peter Wuerfel (Univ. of Karlsruhe, Germany)

CALL FOR PAPERS – ABSTRACTS

Contributed abstracts as poster presentations are encouraged. Abstracts must be no more than one page in length. The abstract should be typed in English, single spaced using Times New Roman style 12pt. A poster presentation is obligatory for grant applicants. The abstract deadline for grant applicants is June 15, 2004 and for regular participants July 15, 2004. The abstracts should be uploaded via conference web page or sent as an e-mail attachment to europv2004@paris.fe.uni-lj.si in MS Word format. Please note that there will be no proceedings from this research conference – only a book of abstracts. New ideas and results discussed at this conference should not be cited in publications without the explicit permission of their author.

DEADLINES

Deadline for grant applications: June 15, 2004
Grant notification: June 30, 2004
Deadline for pre-registration: July 15, 2004

ON-LINE REGISTRATION

<http://www.pv-net.net/europv2004.html>